AN ABSTRACT OF THE THESIS OF

L Roy Bonner IV for the degree of Master of Science in Ocean, Earth, and Atmospheric Science presented on June 6, 2017.

Title: Using EarthScope Magnetotelluric Data to Improve the Resilience of the US Power Grid: Rapid Predictions of Geomagnetically Induced Currents

Abstract approved: _____

Adam Schultz

Geomagnetically Induced Currents (GICs) are quasi-DC signals that are induced in the ground during geomagnetic disturbances (GMDs) and pose a large threat to power grid infrastructure. The power industry currently attempts to mitigate GIC effects by utilizing 1-D ground electrical conductivity based electric field predictions, though conductivity can vary in all 3 spatial dimensions by at least 3 orders of magnitude. These variations can cause predictions to deviate from measured values greatly, which suggests that the resulting GIC predictions can be highly incorrect in areas of conductive heterogeneity. 3-D computational techniques, such as solving Maxwell's equations for electric fields associated with GMDs, can improve prediction accuracy, though they are currently too computationally intensive and slow for industrial use. A computationally light algorithm that implements 3-D magnetotelluric data is proposed and compared to the industry standard method for both electric field and GIC predictions. The algorithm, which is called the Cascading Linear Filter Algorithm (CLFA), utilizes concurrent magnetic time series data from publicly available NSF EarthScope Program sites and United States Geological Survey magnetic observatories to construct observatory-to-site transfer functions. These transfer functions project real-time magnetic field observatory data into predictions for sites within the EarthScope array. Real-time site magnetic field predictions are then projected through 3-D site impedances to yield real-time electric field predictions, which can be interpolated onto points representing the tested power system. GIC based parameters for the power system, and the corresponding electric field at points along the system, are then input into power flow solvers to obtain GIC predictions. Electric field predictions for the CLFA and

industry standard method are compared to measured site values to assess the accuracy of both techniques, and limitations are addressed. GIC predictions resulting from both electric field prediction methods are also compared for three test cases to estimate the impact of implementing the CLFA method on power grid resilience.

Using EarthScope Magnetotelluric Data to Improve the Resilience of the US Power Grid: Rapid Predictions of Geomagnetically Induced Currents

by
L Roy Bonner IV

A THESIS

submitted to

Oregon State University

in partial fulfillment of
the requirements for the
degree of

Master of Science

Presented June 6, 2017
Commencement June 2017

Master of Science thesis of L Roy Bonner IV presented on June 6, 2017

APPROVED:

Major Professor, representing Ocean, Earth, and Atmospheric Science

Dean of the College of Earth, Ocean, and Atmospheric Science

Dean of the Graduate School

I understand that my thesis will become part of the permanent collection of Oregon State University libraries. My signature below authorizes release of my thesis to any reader upon request.

L Roy Bonner IV, Author

ACKNOWLEDGEMENTS

I would first like to acknowledge my advisor Dr. Adam Schultz for his guidance and assistance throughout the research process, while still managing a seemingly impossible schedule. Dr. Schultz served as a shining example of the joy and efficiency that could result from workaholism, which I drew inspiration from during the arduousness of research and deadlines. I would also like to thank my committee members Dr. Eduardo Cotilla-Sanchez, Dr. Gary Egbert, and Dr. Albrecht Jander for their help in the thesis review and defense proceedings. Dr. Cotilla-Sanchez aided in aspects of the GIC prediction portion of my research, in addition to his useful classes on the power industry that I will no doubt utilize in my career. Dr. Egbert's processing classes helped greatly with the coding portions of my research, in addition to his Fortran code serving as a guide for how I constructed my own code. Esteban Bowles-Martinez, Naoto Imamura, and Brady Fry provided helpful feedback during lab meetings as well. I would also like to thank my friends and family for their advice and support throughout my graduate program. My Graduate Teaching Assistantship offered by the College of Earth, Ocean, and Atmospheric Science at Oregon State University was vital in supporting myself and my research, in addition to being a fulfilling job experience.

TABLE OF CONTENTS

TABLE OF CONTENTS (CONTINUED)

LIST OF FIGURES

LIST OF FIGURES (CONTINUED)

1 General Introduction

Given that the third chapter is a continuation of the second and thus both chapters cover the same topics, the material will not be reiterated here to save from redundancy. The main topics that are covered in both chapters are the properties and importance of Geomagnetically Induced Currents (GICs), the principles of magnetotellurics (MT), and the computational procedure for the industry standard and Cascading Linear Filter Algorithm (CLFA) electric field prediction methods. The third chapter also adds principles for calculating GIC effects based on the electric field, as well as the power flow solution parameters that were used to predict GICs.

1.1 Organization

Chapter 2 establishes the data flow for the CLFA method and tests it for a variety of cases to address error and limitations. The CLFA and industry standard electric field prediction method are also compared to site measurements for stations located within an area of heterogeneous electrical conductivity to assess accuracy of both techniques and quantify the effect of limitations within the industry standard method. Chapter 3 builds off of the conclusions from Chapter 2 to associate the industry standard limitations to GIC prediction discrepancies between the two methods in three test cases. Data products resulting from the CLFA method are analyzed in relation to these discrepancies to draw implications concerning the industry method, and conclusions involving grid resilience for both techniques are established. Chapter 4 ties the preceding chapters together to reach a final conclusion about the utility of the CLFA method and its potential to protect the power grid from the effects of GICs.

2 Rapid prediction of electric fields associated with geomagnetically induced currents in the presence of three-dimensional ground structure: Projection of remote magnetic observatory data through magnetotelluric impedance tensors

L R. Bonner IV and Adam Schultz

Space Weather
Issue Number 15

Abstract

Ground level electric fields arising from geomagnetic disturbances (GMDs) are used by the electric power industry to calculate geomagnetically induced currents (GICs) in the power grid. Current industry practice is limited to electric fields associated with 1-D ground electrical conductivity structure, yet at any given depth in the crust and mantle lateral (3-D) variations in conductivity can span at least 3 orders of magnitude, resulting in large deviations in electric fields relative to 1-D models. Solving Maxwell's equations for electric fields associated with GMDs above a 3-D Earth is computationally burdensome and currently impractical for industrial applications. A computationally light algorithm is proposed as an alternative. Real-time data from magnetic observatories are projected through multivariate transfer functions to locations of previously occupied magnetotelluric (MT) stations. MT time series and impedance tensors, such as those publically available from the NSF EarthScope Program, are used to scale the projected magnetic observatory data into local electric field predictions that can then be interpolated onto points along power grid transmission lines to actively improve resilience through GIC modeling. Preliminary electric field predictions are tested against previously recorded time series, idealized transfer function cases, and existing industry methods to assess the validity of the algorithm for potential adoption by the power industry. Some limitations such as long-period diurnal drift are addressed, and solutions are suggested to further improve the method before direct comparisons with actual GIC measurements are made.

2.1 Introduction

Geomagnetically induced currents (GICs) are quasi-DC signals that result from GMDs that perturb the Earth's electric and magnetic field through inductive coupling between

ionospheric (source) currents and currents induced in response in the oceans, crust, and mantle. GICs are capable of causing significant structural damage to pipelines and other built infrastructure through corrosion, and they can severely impact electric power transmission grids through premature aging and failure of transformers [Pirjola et al., 2000b]. In the case of electric power systems, strong currents are able to enter the grounding of transformers and saturate the cores, which can distort the AC waveform of the power signal, leading to a host of other problems such as system relay interference, reactive power loss, or even total system collapse [Molinski, 2002]. There are several examples of geomagnetic storms that have caused GIC-related damage to power grids and to cabled communications systems; the two most widely known being the Carrington event in 1859, where induced currents caused widespread damage to telegraph infrastructure across Europe and North America, and the Hydro-Quebec blackout of 1989, which left Quebec without power for 9 h and almost cascaded across the eastern seaboard of the United States [Boteler et al., 1998], resulting in half-cycle saturation of and serious damage to a nuclear unit transformer in Salem, New Jersey. A variety of factors control the strength of GMDs, such as the 11 year sunspot cycle, episodic coronal mass ejection patterns, and seasonal magnetic field coupling that are capable of combining constructively, so the threat to power resilience is both continual and grave. In particular, a 100 year GIC scenario is estimated to potentially produce ground level electric fields at high geomagnetic latitudes ranging from 5 to 20 V/km, depending on ground (crust and mantle) electrical conductivity structure [Pulkkinen et al., 2012; Love et al., 2016], which could cause serious damage to increasingly integrated and vital electrical systems.

GICs are particularly strong at high latitudes where extreme electromagnetic field events associated with auroral excitations and electrojet currents are more prevalent [Ngwira et al., 2013] and where continental shield areas (e.g., Canadian Shield and Fennoscandia) contain blocks of electrically resistive crustal sections [Cherevatova et al., 2015] that tend to intensify ground electric fields. At lower geomagnetic latitudes GICs can also be driven by interplanetary events such as coronal mass ejections (CMEs) and corotating interacting regions [Kataoka and Pulkkinen, 2008]. CMEs are the major causes of large GIC events [Kataoka and Pulkkinen, 2008], so the problem is fairly universal across a wide range of latitudes and time periods. Even within relatively uniform regional fields [Pulkkinen et al., 2015] there can be amplification of local peaks during severe GMDs [Ngwira et al., 2015] that increase the possibilities for

significant GIC events that can be challenging to predict. For these reasons, researchers have actively investigated methods of mitigating GIC effects to protect power grids. Physically preventing the currents from entering power systems by adding series capacitors can harden sections of the grid against GIC-related damage, although doing so is expensive and tends to divert current to portions of the grid that are not protected, which can create GIC events downstream of the protected grid sections [Pirjola et al., 2000a].

GICs are often difficult to predict, so related factors have been considered as analogs to GICs with varying success, such as horizontal magnetic field changes [Viljanen et al., 2004; Weigel et al., 2002], solar wind patterns [Pulkkinen et al., 2007b; Lotz and Cilliers, 2015], and ionospheric modeling [Pulkkinen et al., 2003; Viljanen et al., 1999]. These related techniques have mainly provided insight into GIC trends rather than being applied to operational predictions, though they have proved to be invaluable in building up GIC methods. There have also been examinations into past GIC events through the work of Wei et al. [2013] and Pulkkinen et al. [2005] to determine GIC causes and test how certain prediction methods would have worked if used at the time. Recent studies have been aimed at detecting GICs through means such as solving coupled ionospheric and surface equations [Love and Swidinsky, 2014], vertical magnetic effects [Vanhamaki et al., 2013], and inversion [de Villiers and Cilliers, 2014]. These techniques have typically been accurate, although too slow and computationally intensive for direct application by industry.

Applied research efforts have been aimed at understanding the nature of GICs to predict and effectively mitigate them through dynamic control of the grid as an alternative to widespread hardening of transformers. GIC prediction software has been developed to model in near real time the effects within a power system of changes in the electric field at ground level due to GMDs [Overbye et al., 2012; Khosravi and Johansson, 2015], so that voltages within the system can be biased to lessen harmful effects. The GIC prediction problem
reduces the components of the specified grid to an equivalent complex circuit, and it uses the ground electric field along the components of the grid to determine the variable intensity of current flow in response to the imposed electric field [Pirjola, 2002]. This approach is already used within the power industry, but current practice is limited to applying electric fields associated with induction in a crust and mantle where the electrical conductivity is 1-D [Pulkkinen et al., 2007a], i.e., it is permitted to vary only with depth. The Electric Power

Research Institute (EPRI) has published a set of regional 1-D conductivity models [Electric Power Research Institute (EPRI), 2002] that are employed for this purpose by industrial GIC prediction codes.

There is growing recognition that the electrical conductivity of the crust and mantle varies strongly in all three spatial dimensions [Kelbert et al., 2012; Meqbel et al., 2014; Schultz et al., 2014; Evans et al., 2014], and that 3-D conductivity variations can lead to significant intensification of ground electric fields [Thomson et al., 2005; Bedrosian and Love, 2015; Love et al., 2016]. Solutions to calculating ground electric fields in the time domain that are related to GMDs for the coupled ionospheric-Earth 3-D induction problem often employ finite difference time domain solutions in massively parallel computing environments [e.g., Simpson, 2009]. At present such solutions are several orders-of-magnitude slower than real-time even on the largest available high performance computing systems. This presents a barrier to the industrial adoption of realistic 3-D ground conductivity models for purposes of GIC prediction. In contrast, solutions that follow current industry practice, based on 1-D regional approximations to ground conductivity, are sufficiently fast to be of practical use. The accuracy of such solutions hinges on the integration of the ground electric field along the path of a power transmission system, which might tend to average out 3-D effects, but the general suitability of this approach remains an open topic of research. In the present work we consider an alternative method by which nonuniform ground electric fields and their associated GICs may be determined rapidly and to reasonable accuracy when induced by GMDs above a 3-D Earth. We also address the inadequacy of the 1-D approximation for a real-world example of estimating ground electric fields.

While now embedded in industry practice, the compendium of regional-scale electrical conductivity models of the crust and mantle organized in the EPRI report is based on information that predates the widespread and systematic installation of magnetotelluric (MT) stations across the continental U.S. through the support of the National Science Foundation funded EarthScope Program [Schultz, 2009]. Other large MT array data sets are also being acquired or have recently been acquired elsewhere in the world [Jones et al., 2008; Thiel et al., 2016], so the method reported in this work may be broadly applicable. The MT method is described in more detail in section 2.2 of this paper. The results of 3-D inversion of EarthScope MT data collected on a grid of stations separated by no more than ~70 km, and in some cases more tightly spaced, have revealed crust and mantle structure that vary laterally on local, regional, and continental

scales by more than 3 orders of magnitude at any given depth [Evans et al., 2014; Kelbert et al., 2012; Meqbel et al., 2014; Schultz et al., 2014]. Most important for purposes of GIC prediction, the EarthScope 3-D conductivity images of the crust and mantle [e.g., Meqbel et al., 2014] bear little resemblance to the regional 1-D conductivity profiles contained with the EPRI report [EPRI, 2012]. This discrepancy between 1-D and 3-D images of conductivity structure has significant impacts on both the intensity and direction of ground electric fields and associated GICs that would arise during a given GMD.

2.1.1 Predicting Ground Electric Fields Through the Magnetotelluric Impedance Tensor

Electrical conductivity models of the Earth's crust and mantle are usually obtained by inverse modeling of electromagnetic transfer functions that describe the relationship between the magnetic and electric fields at or near the Earth's surface. In the magnetotelluric (MT) method for generating such models, measurements of orthogonal vector components of the naturally occurring time variations in the electric and magnetic fields at ground level are obtained over a period of time. The duration over which the data are measured depends on the depth of interest for the study, since the depth of penetration into a conducting Earth of incident time-varying magnetic fields scales inversely with the frequency of the signal, so long-period magnetic field variations penetrate to greater depth than short-period variations. As the time-varying magnetic fields diffuse into the crust and mantle, electric fields are induced, converting some of the energy of the incident magnetic fields into electric currents, thereby progressively attenuating the down-going magnetic fields with increasing depth. At ground level, the time-varying magnetic fields are predominately of ionospheric (source current) origin, with a fraction of the energy associated with secondary magnetic fields that diffuse up to the surface from the induced electric currents. The time-varying electric fields at ground level are predominately associated with the induced fields, which are related to the inducing magnetic fields by the electrical conductivity distribution within the subsurface. Frequency therefore serves as a proxy for depth, so the electric and magnetic vector component time series are transformed into the frequency domain through Fourier transformation, and a set of transfer functions that relate the field components to each other is obtained.

The most common form of transfer function used for magnetotelluric inverse modeling, the MT impedance tensor, is a frequency-dependent quantity that relates the orthogonal horizontal components of the electric fields to the orthogonal horizontal components of the magnetic fields at each measurement site

$$\begin{pmatrix} \boldsymbol{E_x^f} \\ \boldsymbol{E_y^f} \end{pmatrix} = \begin{pmatrix} \boldsymbol{Z_{xx}^f} & \boldsymbol{Z_{xy}^f} \\ \boldsymbol{Z_{yx}^f} & \boldsymbol{Z_{yy}^f} \end{pmatrix} \begin{pmatrix} \boldsymbol{H_x^f} \\ \boldsymbol{H_y^f} \end{pmatrix} + \boldsymbol{U^f}, \qquad \textbf{(2.1)}$$

where E represents the complex-valued Fourier coefficients of the electric field, H the complex-valued Fourier coefficients of the magnetic field, Z the complex-valued impedance, U the incoherent noise, x and y the north and east directions, respectively, and f represents a given frequency. Written in this form, the impedance Z is a complex-valued frequency domain tensor that can be used to project the magnetic field variations (a vector of a given magnitude and direction) at a given location on the Earth's surface and at a given frequency into the corresponding variations of the vector electric field for that location and frequency [Telford et al., 1990].

MT data are typically obtained through deployments of a number of temporary observing stations. In order to obtain data that yield electrical conductivity information on crust and mantle structure to depths of ~10 km – ~350 km below ground level, MT impedances must be known over the frequency band of ~10^{-4} Hz – ~10^{-1} Hz. To achieve this, each MT station typically operates for 10 d – 30 d at a given location within the survey grid, depending on the level of geomagnetic activity and the conductance of the upper crust, factors that can impact the generation and attenuation of MT signals. Once MT data of sufficient quality and duration have been obtained at each site, the station is moved to another location on the survey grid and the process is repeated.

The classical MT method assumes that ionospheric signal sources are sufficiently distant to be considered plane waves [Cagniard, 1953]. While the plane wave assumption is generally valid, it breaks down at high geomagnetic latitudes near the conjugate auroral ovals and beneath the ionospheric equatorial electrojet, so classical MT processing methods [e.g., Egbert and Booker, 1986] that are resistant to the influence of a mild degree of non-plane wave sources on the impedance estimation process are restricted to a broad range of midlatitudes [Wait, 1962], and methods that accommodate persistent and energetic non-plane wave sources must be adopted

for those other regions [Imamura and Schultz, 2015]. The resulting frequency domain MT transfer functions typically contain information within each frequency band that is gathered from a wide range of source (inducing) magnetic field orientations. The calculated impedance tensors therefore represent the scaling between source magnetic fields and the electric fields that arise in response to these magnetic fields. This scaling should be valid for any plane wave magnetic field polarization within the frequency bands for which impedance elements have been obtained.

For scenarios where the ground conductivity varies only with depth (i.e., a 1-D Earth), the diagonal elements of the impedance tensor are zero and the off-diagonal elements are of equal magnitude and opposite sign. In this case the horizontal electric and magnetic fields in the Earth that are induced in response to GMDs remain mutually orthogonal regardless of frequency, polarization of ionospheric source fields, or location within the observation grid. In contrast, for a 3-D conducting Earth, all four elements of the impedance tensor may be nonzero, the relative orientation of the electric and magnetic field vectors can be nonorthogonal, and the direction and intensity of the ground electric field can vary dramatically at different frequencies, for different source field polarizations, and at different grid locations within a survey region. In the 3-D situation, even a small change in the orientation of the ionospheric source magnetic field during the course of a GMD can produce potentially large changes both in the intensity and orientation of the resulting ground electric fields. This is not the case for a 1-D conducting Earth.

Furthermore, ground electric fields resulting from a GMD of a given magnitude and source magnetic field orientation can be intensified substantially (by up to an order of magnitude) for the 3-D case relative to the 1-D case [Thomson et al., 2005; Bedrosian and Love, 2015; Love et al., 2016] and can vary dramatically in direction and intensity from one GMD to another since the time-frequency content of source field intensity and orientation is unique to each GMD. An important consequence of this is that no general linear scaling exists between the ground electric fields predicted from a GMD acting on a 1-D conductivity model and those predicted from a 3-D model.

2.2.1 Electric Field Distortion and Impacts on Predicting Electric Fields From Magnetic Fields

The impedance tensor Z (equation (2.1)) is a linear filter that projects the magnetic field at a given site into the electric field at the same site, for any source polarization and for any

frequency within the bands for which it is defined. The impedance tensor therefore contains all information necessary to undertake local field projection, which includes but is not limited to all known information about the electrical conductivity structure within the range of depths of penetration associated with the frequency content of Z.

MT data have finite spatial resolving power, which is determined by the actual subsurface electrical conductivity structure, the spatial extent and interstation spacing of the MT measurement array, and by the frequency content of and statistical confidence limits on the MT transfer functions used in the inversion. At depths shallower than a critical depth determined by the subsurface conductivity structure and by the highest-frequency data available, there is essentially no structural resolving power and the MT method becomes insensitive to the structural details, although it remains sensitive to the bulk conductance (vertically integrated conductivity) of those shallow layers. It is well known, however, that the electric field can be distorted at all frequencies by the presence of near-surface heterogeneities (i.e., fine-scale 3-D structure of arbitrary complexity that is too small to be resolved by the MT data). The effect of these shallow "scattering layers" is to change the scaling between electric and magnetic fields at a given site [Bahr, 1988], even when the magnetic field within a survey area is broadly uniform [Pulkkinen et al., 2015], and even if the underlying deep electrical conductivity structure is also broadly uniform or even 1-D. In addition to information about deeper electrical conductivity structure, the measured impedance tensor also contains information about such "static distortion" effects, which can vary from site to site independently of the underlying, deeper 1-D, 2-D, or 3-D conductivity structure information that is also contained within the impedance tensor.

Prior to inverting Z to obtain a 1-D or a 2-D ground conductivity model, shallow 3-D static distortion effects are typically removed from the impedance tensor using one of a series of "tensor stripping" operators [e.g., Groom and Bailey, 1989; Jones, 2011]. The modified or stripped tensor is then used for inverse modeling of the ground conductivity structure, free from the complications of the surface scattering layer. In the Groom and Bailey formulation, the undistorted or stripped impedance tensor may be given by

$$\mathbf{Z}_m = g\,\mathbf{R}\,\mathbf{T}\,\mathbf{S}\,\mathbf{A}\,\mathbf{Z}_2\,\mathbf{R}^T, \tag{2.2}$$

where Z_m is the measured impedance tensor, g is the "site gain," which is a scalar, R is a rotation matrix, T and S are "twist" and "shear" tensors, respectively, A is the "anisotropy" or "splitting" tensor, and Z2 is the undistorted or "stripped" tensor. The subscript for Z2 refers to Groom and

Bailey's assumption that there is an underlying or regional two-dimensional structure with a principal electrical strike direction beneath the distorting 3-D surface layers. The rotation matrix acts to align the undistorted matrix with the principal axes of that 2-D structure.

While this process has proven essential for 1-D and 2-D inversion for ground conductivity, there are differing opinions about the necessity of removing the distorting effects of unresolvable, shallow 3-D scattering layers prior to inversion of impedance tensors in fully 3-D environments. Methods have been developed for distortion removal [e.g., Utada and Munekane, 2000] prior to 3-D inversion, whereas others allow for shallow 3-D scattering layers in their 3-D models [Kelbert et al., 2012] that, while containing model cells that fall far below the resolving limits of the MT data set, may be used to express the galvanic distortion effects on the electric field.

The concept of tensor stripping has an important consequence for those applying ground conductivity models to the GIC prediction problem. Methods that solve for the ground electric fields, given a known conductivity model that have first stripped out the effects of the shallow 3-D scattering layer (which is generally the case for published 1-D and 2-D models, and can be the case for some 3-D models), will produce undistorted ground electric fields, with the effects of static distortion removed. Such electric fields differ from those actually measured at each site, since the real-world electric fields are distorted by fine-scale heterogeneities in near-surface conductivity structure, whereas the MT-derived conductivity models typically have such effects removed. Efforts to use ground conductivity models based on tensor stripped impedances will yield ground electric field predictions that will not, in general, match the measured electric fields on the ground. This point is not generally recognized in the GIC prediction literature.

Efforts to empirically adjust ground electric field predictions, such as those based on regional 1-D ground conductivity models, by calculating a heuristic scaling factor to minimize the misfit between observed and calculated GICs are essentially equivalent to efforts to estimate g, the site gain factor in equation (2.2), independent of the other distortion tensors. By disregarding the other distortion factors, such an approach cannot adequately account for the rotation, shear and twist effects on the electric field due to the shallow 3-D scattering layers, which are ubiquitous even when the deep underlying structure is not 3-D. Since the electric field is a vector field, disregarding either shallow 3-D distortion effects or deeper 3-D crust and

mantle conductivity effects, or both, can significantly bias both the magnitude and the direction of the resulting ground electric field.

For the work reported here, based on using unstripped impedance tensors, these issues are not a factor. It is also not a factor when using 3-D electrical conductivity models to predict the ground electric field for the subset of 3-D models developed using unstripped impedance tensors and where a shallow galvanic scattering layer is an explicit component of the model, as opposed to those 3-D models that lack this layer and that are derived from inversion of stripped impedance tensors.

2.2.2 Projecting the Contemporary Magnetic Field on to Previously Occupied MT Measurement Sites

For operational GIC prediction, the magnetic fields must be known at multiple points along the path of the power distribution system in near real time, whereas the MT stations used to estimate Z at a set of locations are, in general, no longer operating nor situated directly along power line paths. While it is common practice in GIC research to apply a simple geomagnetic latitude scaling factor to represent the geographic dependence of GMD magnetic field intensity, we propose a different approach. We hypothesize that magnetic fields recorded by magnetic observatory networks, such as those operated by the U.S. Geological Survey (USGS) or equivalent agencies around the world, can be projected on to the locations of previously occupied MT stations by construction of frequency domain transfer functions that relate the magnetic field variations at one or more magnetic observatories to the magnetic field variations that were actually recorded at each of the MT observation sites during the same period of time. We further posit that once determined, the transfer functions can be used to project real-time magnetic field variations data from those observatories into real-time predictions of the magnetic field at each of those sites. The MT impedance tensors associated with each site (which contains all known information about 3-D conductivity structure beneath and surrounding those sites, including shallow distortion/surface scattering effects) can then be used to project the real-time predictions of the magnetic fields at those sites into real-time predictions of the ground electric fields. These can then be interpolated from the MT station locations onto the locations of the power distribution lines.

The MT data necessary to test this hypothesis were collected from a temporary MT array spanning western Oregon and southwestern Washington, shown in Figure 2.1, under the support of a National Science Foundation (NSF)-funded joint EarthScope-GeoPRISMS project EAR-1053632, “Onshore-offshore MT Investigation of Cascadia Margin 3-D Structure, Segmentation and Fluid Distribution,” along with magnetic observatory data collected by the USGS. Electric field components at the MT array sites were determined from geomagnetic north-south (x) and east-west (y) oriented 100m long dipoles that consisted of cables linking pairs of grounded Pb-PbCl2 electrodes, and the magnetic field components were measured via sensitive, observatory quality Narod Geophysics triaxial ring-core fluxgate magnetometers that were oriented toward geomagnetic north. Narod Intelligent Magnetotelluric Systems recorded time series of each of the electric and magnetic field vector components at 1 s intervals. The effects of local cultural electromagnetic noise on the measured impedance tensors were reduced through remote reference processing [Gamble et al., 1979]. Short data gaps were removed, and the influence of nonstationary and non-plane wave signal sources was minimized using methods enumerated in Jones et al. [1989] and Egbert and Booker [1986].

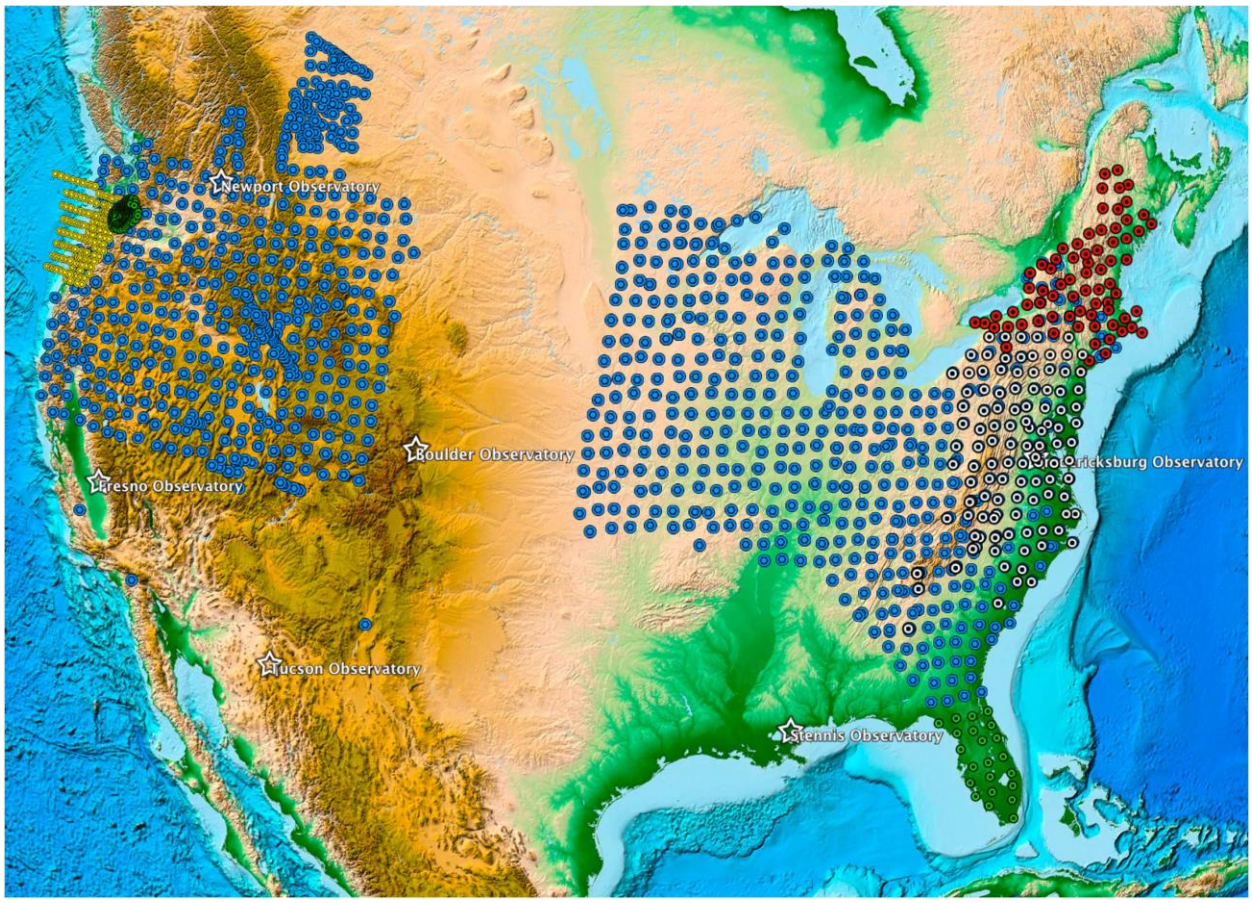

Figure 2.1: Locations of NSF EarthScope Program Magnetotelluric Transportable Array (MT TA) stations. Stations completed between 2006 – 2015 are shown as blue dots (the Peninsular Florida stations were acquired by the US Geological Survey [P. Bedrosian, pers. comm., 2016], the Canadian stations by the University of Alberta [M. Unsworth, pers. comm., 2011], and the higher density cross-shaped array centered on western Wyoming by the University of California, San Diego [C. deGroot-Hedlin, pers. comm., 2009]; all other sites were EarthScope MT TA sites acquired on a nominal 70 km station spacing grid under the direction of Oregon State University). EarthScope MT TA stations completed under the direction of Oregon State University in 2016 (white dots), and currently being installed and planned for completion by Oregon State University in 2016-2017 (red dots).

In contrast to the temporary MT array data, magnetic observatory data are collected continuously and adjusted for baseline shifts due to instrument drift, whereas temporary MT station data are collected for a limited time period and do not adjust for such shifts, thereby restricting the usable frequency bandwidth to a practical low-frequency limit of ~10^{-4} Hz in most cases. This restricts the sensitivity of the MT data to mantle depths of $\lesssim$350 km below ground level. If the need arises, deeper conductivity information can be obtained using other methods [e.g., Kelbert et al., 2009], although these provide 3-D information of lower spatial resolution than MT-based results.

A hallmark of MT data obtained under NSF EarthScope support is its availability to the general public without restriction [Kelbert et al., 2011], the provision of pre-calculated impedance tensors as well as time series, and the geographic scope of the EarthScope MT Program (Figure 2.1) with a grid of stations with nominal 70 km station spacing. In some cases, higher-resolution MT data with closer station spacing (such as that shown in Figure 2.2) exist separate from the EarthScope MT Transportable Array shown in Figure 2.1. The EarthScope Program ends in 2018, and additional MT stations will supplement those shown in this figure in the intervening time, with plans to extend the southern extent of the array that currently covers the north-west quadrant of the U.S., by adding two to three rows of stations and with the possibility of a sparser array of sites to be installed in the Great Plains to bridge the two large existing MT arrays seen in the figure. By the conclusion of the EarthScope Program, half of the area of the continental U.S. will be covered by long-period MT data.

The wide geographic scope of these open-access data sets opens up the possibility that the method demonstrated in the present work can be broadly applied across the territory of the U.S., and in areas where other large-scale MT array data exist, more globally as well. In areas where no such MT data exist, it is feasible to expand upon the existing EarthScope MT array to acquire MT impedance tensor information in areas of interest to the electric utilities.

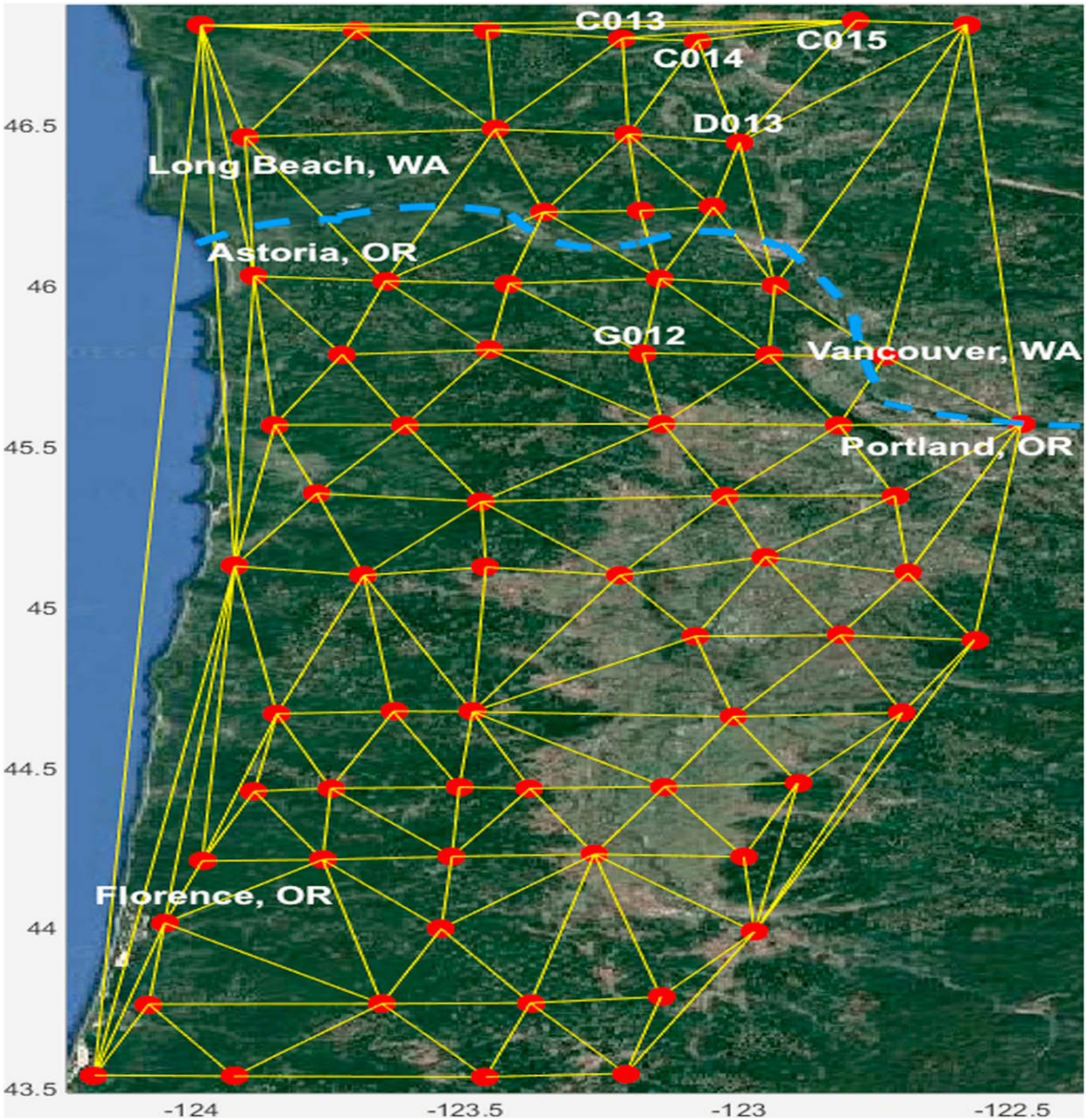

Figure 2.2. Map of the Delaunay triangulation formed by using the western Oregon and southwestern Washington portion of the EarthScope-GeoPRISMS project EAR-1053632 MT array sites used in the present work (these comprise most of the land MT stations that appear as small yellow symbols in Figure 2.1). The area displayed extends north-south ~370 km and east-west ~130 km, northward to just south of the Olympic Peninsula and just west of Seattle in the state of Washington, south to approximately the latitude of Coos Bay at the southern Oregon coast, and from the Pacific coast to the west and the foothills of the Cascade volcanic range to the east. The dashed blue line marks the border between Washington and Oregon, along the path of the Columbia River. In contrast to the EarthScope MT Transportable Array stations shown in Figure 2.1 with their nominal 70 km station spacing (blue, white, and red symbols), for this project the station density was approximately three times finer. The MT station locations are at the vertices of the Delaunay triangles, marked by a red dot. The axes are marked in degrees of latitude (y axis) and longitude (x axis), respectively. The identification of the nearestcneighboring MT stations to any location within the MT array, such as the path of power lines, is based on construction of Delaunay triangles, as shown here and discussed in sections 2.3 and 2.4 of this paper.

2.3 Algorithmic Considerations

Electric field predictions along the path of a transmission line can be generated by projecting a real-time stream of magnetic observatory data through observatory-to-MT site magnetic field transfer functions and then by projecting the resulting predicted magnetic fields at each of the previously occupied MT stations through the impedance tensors calculated from previously collected EarthScope data. Doing so produces electric field predictions at the corresponding (former) MT measurement sites, which can then be interpolated from the MT array locations onto points representing the transmission line. The values of the vector ground electric field for each of these points can then be integrated to obtain the total ground electric field along the line, which is necessary for GIC calculations and damage mitigation. The data flow from magnetic observatory data to total electric field predictions is shown below in Figure 2.3.

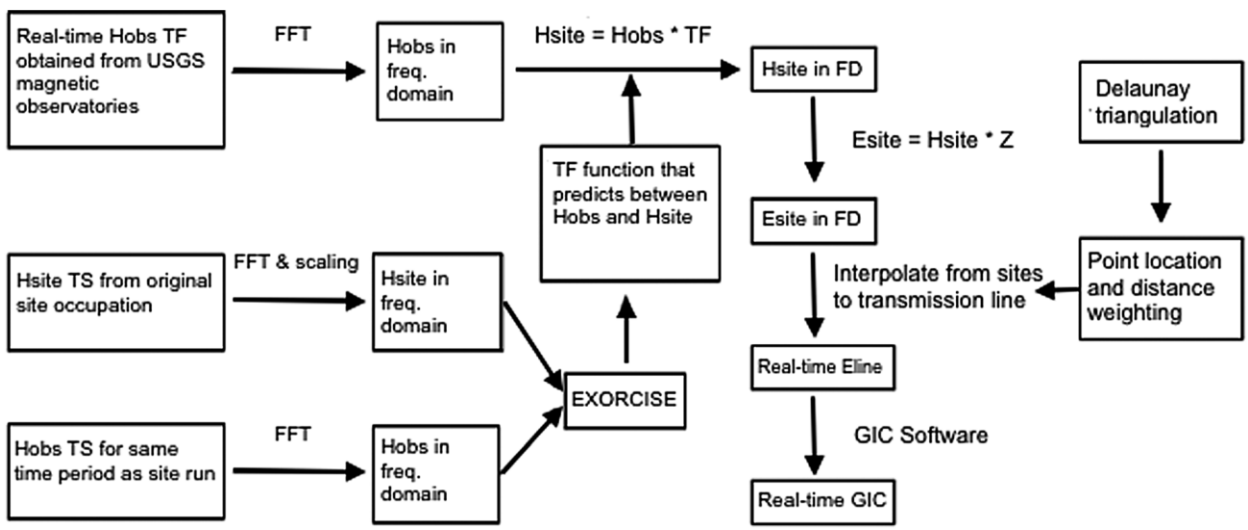

Figure 2.3. Data flow chart of computations necessary to transform real-time magnetic time series into predicted total electric field values for GIC predictions, where FFT indicates fast Fourier transformation, TS are the time series, and FD indicates frequency domain.

The first step involves determining a transfer function for each MT station whose input signals consist of the vector magnetic field variations recorded at one or more magnetic observatories, and whose output signals are the vector magnetic field variations that were actually recorded during the operation of each MT station. The observatory and MT station time series must be synchronous and concurrent, with identical sample intervals. Accuracy is

improved when nearby observatories are included that surround and effectively bound the MT station array.

For the example reported here, utilizing MT array data that span much of western Oregon and southwest Washington in the United States (Figure 2.2), the USGS magnetic observatories chosen were Newport Washington, Boulder Colorado, Fresno California, and Honolulu Hawaii. The closest observatory, Newport, lies approximately 540 km from the center of the MT station array, whereas Honolulu, the most distant observatory, lies approximately 4150 km from the center. Geographically favorable data from the magnetic observatory at Victoria, British Columbia, Canada were not used since a real-time data stream of 1-sample per second data is not currently available from that site, whereas an open source library of Python language [Van Rossum, 2011] scripts has been developed by the USGS Geomagnetism Program [Geomag Library, 2016] that make such data accessible in (near) real time from the USGS magnetic observatory network.

Multistation transfer functions that relate the magnetic field vector components at the set of observatories to the magnetic field vector components at a given MT station were obtained following the algorithm of Zhang and Schultz [1990]. The frequency domain transfer function $\Gamma(\omega)$ that relates data at a local MT station simultaneously to data at a set of one or more remote observatories is given by

$$X_o(\omega) = \sum_{i=1}^{M} \Gamma_i(\omega) X_i(\omega) + \delta X(\omega), \tag{2.3}$$

where $X_0(\omega)$ and $X_i(\omega)$ ($i \neq 0$)are the complex-valued Fourier coefficients of the local and remote components of the vector magnetic fields, ω is the radian frequency ($\omega=2\pi f$, where f is in Hertz), $\delta X(\omega)$ is the uncorrelated residual, $\Gamma_i(\omega)$ is a partial transfer function relating X_0 to X_i, and M is the number of remote observatories. The solution for $\Gamma(\omega)$ is found by minimizing the L2 norm of the residual $\delta X(\omega)$ for each frequency band

$$min\ [\![\delta X(\omega)^2]\!] \ = \ min\ [\![\left|X_o(\omega) - \sum_{i=1}^{NxM} \Gamma_i(\omega) X_i(\omega)\right|^2]\!]\ , \tag{2.4}$$

where the brackets $[\![\,]\!]$ represent a frequency band-averaging operator, and Γ is taken to be invariant within each frequency band. We solve for the transfer function coefficients by QR decomposition of the normal equations. In practice, the calculation of the transfer functions is an iterative process, where in each iteration the residual between the predicted magnetic field at each MT station location is calculated from

$$\delta x_0(t) = x_0(t) - \mathrm{FFT}^{-1}[\sum_{i=1}^{M} \Gamma_i\,(\omega) X_i(\omega)], \tag{2.5}$$

where the inverse Fast Fourier Transform (FFT^{-1}) operator [Cochran et al., 1967] yields a time domain prediction of the magnetic field components at a given MT station location from the Fourier coefficients of the magnetic field components at the remote magnetic observatories as projected through the transfer function and where $\delta x_0(t)$ is the residual between that predicted field component and the measured field component $x_o(t)$ in the time domain. When the magnitude of the residual exceeds a certain threshold, taken by Zhang and Schultz [1990] to be a multiplicative factor of the interquartile deviation around the median value of all residuals, the data point is taken to be an outlier and it is replaced by the predicted value. The process iterates until no additional outliers are detected, as described in more detail in Zhang and Schultz.

Prior to transformation to the frequency domain, short gaps in the time series are interpolated by autoregressive prediction [Janssen et al., 1986; Zhang and Schultz, 1990], and the time series is high-pass filtered to remove energetic diurnal variations typically associated with ground electric and magnetic fields that cause spectral leakage and drift [Stearns and Hush, 1990]. This drift biases the predicted signal and can introduce step discontinuities between adjoining sections of predicted data. The windowed data are then pre-whitened by removal of the mean value and the best fitting linear trend, and then the data section is multiplied by a time domain taper function to minimize spectral leakage between frequency bands. We apply a time-bandwidth product 4 π prolate spheroidal taper function [Chave and Thomson, 2004] for this purpose. A data window length is selected that is sufficiently long to contain multiple cycles of harmonic signals matching the lowest-frequency band found in the MT transfer functions, which is typically 10^{-4} Hz. A minimum of 10 and ideally as many as 100 or more 10,000–20,000 s long sections of time series data are required in order to achieve a statistically acceptable frequency domain representation of these low-frequency signals. Examples are shown later using differing window lengths within this range. As is the case generally for Fourier analysis, it is assumed that the signal is stationary within the time window selected. While the examples shown later suggest the assumption of stationarity leads to excellent predictions, the method introduced here could be refined by applying time-localized analogs to the FFT, such as wavelet or the S transforms [Yun et al., 2013], although this is outside the scope of the present work. Other details of the iterative refinement of the transfer function estimates can be found in Zhang and Schultz [1990].

2.3.1 Interpolating Predicted Fields Onto the Power Transmission Grid

The next step in preparing for real-time predictions involves interpolating ground electric field data from the MT station sites onto points along the path of nearby transmission lines. We make use of a nearest neighbor interpolation algorithm following Schultz and Pritchard [1999]. We construct a Delaunay triangulation [Chew, 1989] of the MT station locations (as seen previously in Figure 2.2), where the MT station locations are the vertices of the triangles. We determine if a given point along a transmission line path is contained within the convex hull of each Delaunay triangle, which is true if the determinant of the point and each vector comprising the triangle is positive, i.e., the point is to the left of each side when going in a counterclockwise direction [Barber et al., 1996]. We determine the great circle distance between each point along the path of the transmission lines and each vertex of the Delaunay triangle that contains the given point. Once the ground vector electric field variations have been predicted at the vertices (each of which is the location of a previous MT station and impedance tensor estimate), the electric field is interpolated onto the transmission line path by averaging the vector electric field values at the three vertices of the Delaunay triangle that encompasses that point, weighted inversely by the distance of each vertex from that point along the transmission line path.

This approach contrasts with methods that directly apply an existing electrical conductivity model of the crust and mantle to the problem of predicting ground electric fields by solving the forward problem of electromagnetic induction for a given source field model in either 1-D, 2-D, or 3-D. The primary difference in approach is that the forward solutions obey the governing equations for electromagnetic induction, whereas our strictly geometrical, nearest neighbor interpolating function does not. On first glance this would seem to be a significant disadvantage to our approach, but one must consider the intrinsic inaccuracies and approximations that go into solving the electromagnetic induction inverse problem to generate a conductivity model. At each point within such a model, the conductivity is discretized to a certain degree, it is known to a given uncertainty, and rather than representing an exact point estimate of the true conductivity at each location, it is a volume-averaged estimate of the conductivity whose spatial averaging function is difficult to establish given the nonlinearity of the inverse problem. Ultimately, such a conductivity model represents a series of propagated

uncertainties at every step of fitting the observed impedance tensor (and, potentially other data as well). As mentioned previously, that model may also omit surface scattering layers that can have a profound impact on the electric field at all frequencies.

In our approach we avoid solving the electromagnetic induction problem and instead consider the impedance tensor strictly as a linear filter that transforms ground magnetic fields into ground electric fields. Since this skips the steps of solving an electromagnetic induction forward problem for a discretized model, we believe there are fewer opportunities for errors to be introduced in the projection of magnetic fields to electric fields at each MT station location. It is an open question whether the next step, the interpolation of predicted ground electric fields onto the transmission line paths, introduces greater errors than the accumulated errors of solving the induction forward problem based on a conductivity model of finite discretization and uncertainty. It is also an open question if there will be a systematic bias from interpolating electric fields that contain local static distortion effects onto the path of the transmission lines, since such distortion may be local to each point along the path. It may transpire that this fine-scale distortion will average out as the ground electric fields are integrated along the transmission line path for purposes of predicting GICs. While we do not have definitive answers to these questions at present, our initial results, provided below, suggest that the geometric interpolation of distant magnetic observatory data through successive transfer functions and impedance tensors is an effective approach.

2.4 Results

The fundamental problem we address in this work is the near real-time prediction of electric fields along the path of power distribution lines without the computational burden of explicitly solving the coupled equations for electromagnetic induction above a known Earth conductivity model. To accomplish this, we employ a set of previous recordings of electric and magnetic fields and previously calculated MT impedance tensors at an array of MT station locations that encompasses the power line pathway. By successively applying a set of linear filters (first, a transfer function that relates distant magnetic field observations to those previously recorded at the MT stations, and then a set of MT impedances that project the local magnetic field variations

into local electric field variations), we seek to show that we can faithfully reproduce the magnetic and electric fields that were actually recorded at the MT stations. Having accomplished that, we then seek to show we can reasonably interpolate the predicted electric fields to any location within the geographic span of the MT array, which would include the paths of the power distribution system of interest. We refer to our approach subsequently in this work as the "Cascading Linear Filter Algorithm," or CLFA.

In this section of the paper, we demonstrate the contributions to the prediction of the electric field variations from each aspect of the CLFA prediction process. First, we examine the impact that distance between the local MT station location and the distant magnetic observatories has on the integrity of the predicted local magnetic fields. We then demonstrate the effectiveness of using such predicted local magnetic fields to generate predictions of the local electric fields by projecting the magnetic fields through the local MT impedance tensors. Finally, we demonstrate that we can use the nearest neighbor interpolation method described in section 2.3.1 to project a set of predicted electric fields from MT station locations surrounding a point of interest and faithfully reproduce the electric field actually recorded at that point.

2.4.1 Projections of Magnetic Fields From a Single Distant Observatory to a Single MT Station

To start, we construct a set of simple transfer functions that project the magnetic field components at a single distant magnetic observatory to those at a single MT site, i.e., we set N = 1 in equation (2.3). Figure 2.4 displays the individual projections of the magnetic field from each of the four magnetic observatories used in this study through such single-station transfer functions, which yields a set of four different predictions of the local magnetic field at the given MT site. This illustrates that the proximity of the magnetic observatories impacts the quality of the fit between observed and predicted magnetic fields. The projected magnetic fields from the closest observatory at Newport, Washington, best match the actual magnetic fields at the MT station (designated site G012, located 50 km northwest of Portland, Oregon, and ~500 km from Newport, Washington), due to the high coherence between the two signals. The coherence between the magnetic fields decreases with greater station separation, in part because of spectral leakage from long-period signals such as diurnal variations that have increasing phase and magnitude difference with increasing distance. Differences aside, by employing multiple remote

magnetic observatories (setting N = 4 in equation (2.3) in this case), improve the overall fit of the predicted magnetic field relative to the single-station case. This will be illustrated in subsequent examples. Observatories with higher coherence with the local signal have a larger impact on the fit of the predictions, which can be problematic if errors in the real-time stream of data from these observatories go undetected during real-time predictions, yet the inclusion of other observatories does improve the fit of the projected magnetic fields.

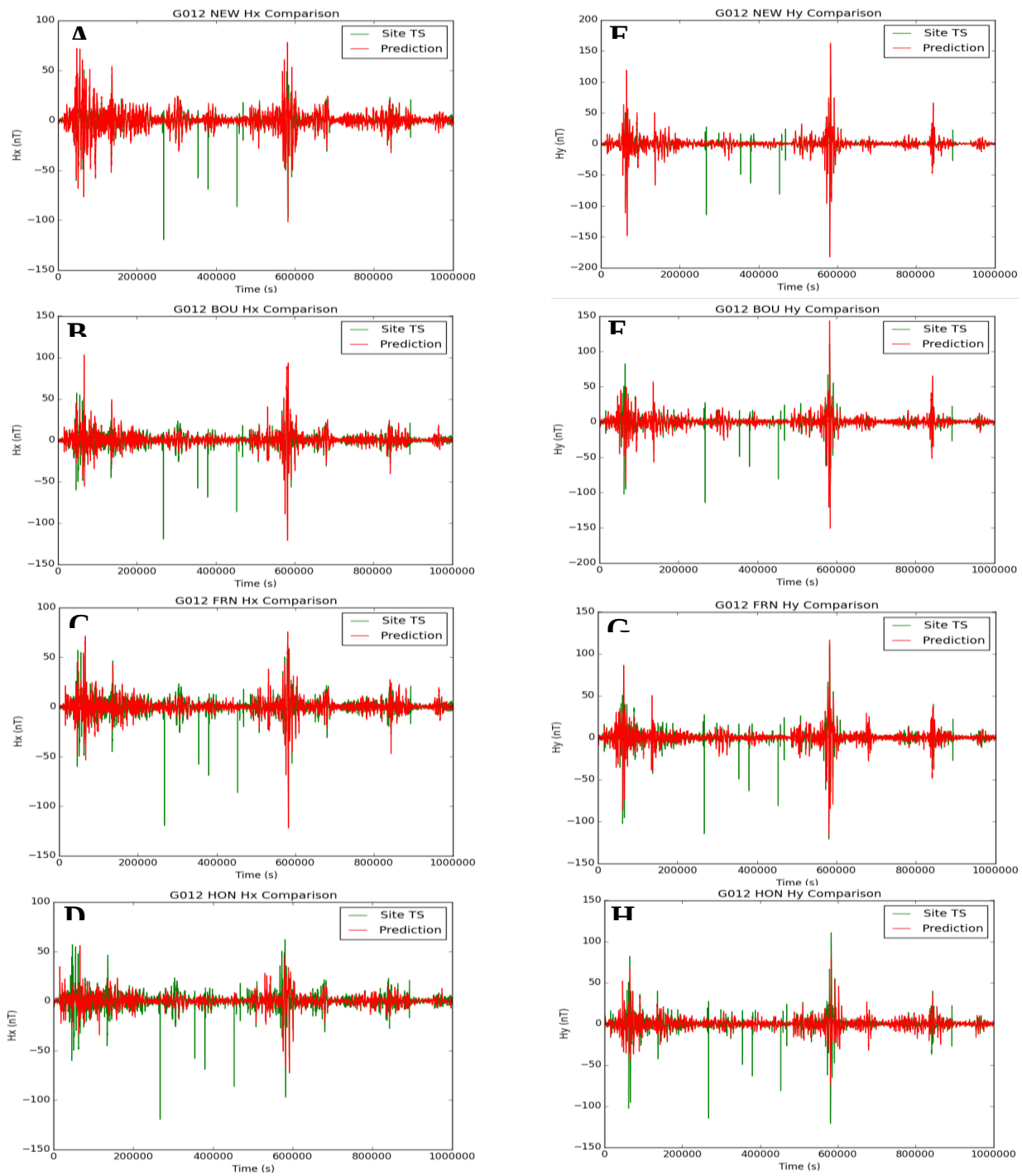

Figure 2.4: Comparisons between the actual recorded (green curves) and predicted (red curves) horizontal components of magnetic field variations time series at MT station G012 near Portland, Oregon based on projections of magnetic fields from individual magnetic observatories through single-station transfer functions. Data from the USGS magnetic observatories at Newport Washington, Boulder Colorado, Fresno California, and Honolulu Hawaii were used in this and other examples throughout this paper. A time series window length of 10^6 s (~11.6 d) is shown. (A) – (D) show the recorded north-south (x) component of the magnetic fields at station G012 and those predicted at that site by projection of data from the remote magnetic observatories at Newport (A), Boulder (B), Fresno (C), and Honolulu (D). (E) – (F) show the corresponding east-west (y) components of the measured and predicted magnetic fields.

We also examine the effect of increasing magnetic observatory distances on the quality of the predicted electric field at an individual MT station (Figure 2.5). As expected, electric field prediction quality degrades with distance as magnetic field prediction errors are propagated through the impedance tensor. Figure 2.5 demonstrates the distance limitations in using only a single distant observatory for electric field predictions. Figures 2.5a and 2.5e show the north-south (x) and east-west (y) recorded and predicted electric fields based on projecting the magnetic fields from relatively nearby Newport observatory, at a distance of ~500 km from the station, over a time period of ~11.6 days. Viewed on this scale, aside from a short duration event at about 550,000 s from the start of this record, the predicted and recorded electric field components conform to within a couple of mV/km or less. More quantitative analysis of the prediction misfits arising from using multiple rather than single observatory data sets will follow, but this serves to illustrate the point that observatory distance impacts the fidelity of the electric field predictions. Figures 2.5b and 2.5f for data projected from Boulder (1546 km from site G012), 2.5c and 2.5g from Fresno (1004 km), and 2.5d and 2.5h from Honolulu (4175 km) show progressively increasing prediction misfits with distance. At the greatest distances electric field prediction misfits are more typically in the 5–10 mV/km range.

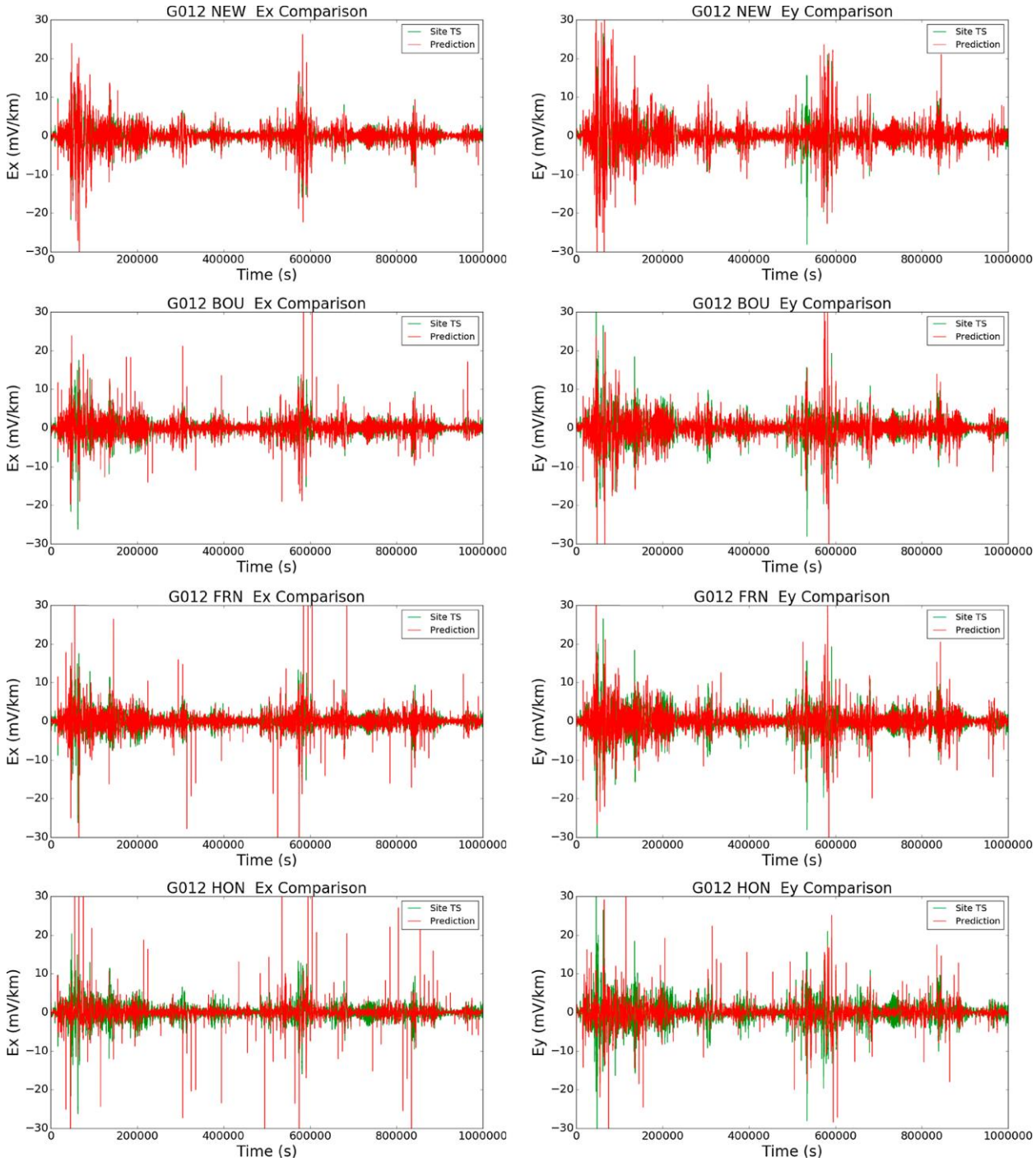

Figure 2.5. Comparisons between the actual recorded (green curves) and predicted (red curves) horizontal components of electric field variations time series at MT station G012 near Portland, Oregon, based on projections of magnetic fields from individual magnetic observatories through single-station transfer functions following which predicted magnetic fields are projected through the impedance tensor for station G012 to yield predicted electric fields. Data from the USGS magnetic observatories at Newport, Washington; Boulder, Colorado; Fresno, California; and Honolulu, Hawaii were used in this example. A time series window length of 106s (~11.6 days) is shown. (a–d) The recorded north-south (x) component of the electric fields at station G012 and those predicted at that site by projection of data from the remote magnetic observatories at Newport (Figure 2.5a), Boulder (Figure 2.5b), Fresno (Figure 2.5c), and Honolulu (Figure 2.5d) and application of the impedance tensor at G012. (e–f) The corresponding east-west (y) components of the measured and predicted electric fields.

2.4.2 Projections of Magnetic Fields From Multiple Distant Observatories to a Single MT Station

Improvements in predicting the magnetic field components at each MT site by simultaneously projecting magnetic fields from four remote magnetic observatories (i.e., setting N= 4 in equation (2.3)) can be seen in Figure 2.6, where the coherence between the measured and predicted time series is apparent, even when viewed in more detail on a much finer timescale (x axis) and field amplitude scale (y axis) than shown previously in Figure 2.4. Given the fine scale of this plot, we show the projected magnetic fields with ±95 % confidence intervals, where the magnetic field transfer function covariances are calculated by adapting Eisel and Egbert's [2001] basic transfer function covariance expression (their equation (11)) to the multiple station magnetic field problem, following which we propagate the uncertainty in the transfer function into the projected magnetic fields by applying classical uncertainty propagation theory [Ku, 1966]. Minor deviations still remain due to limitations with the algorithm, such as the need to group the frequencies into a small number of bands that smooth out the energy contained within any narrowband spectral peaks that might be encountered.

The conditions that produced the lowest misfit predictions, shown in Figures 2.6 through 11, included using a moving 20,000 s data section window tapered by multiplying by a time-bandwidth product 4 π prolate spheroidal taper function with 50% overlap between adjacent time series sections to estimate the Fourier coefficients used for calculating transfer functions and for projecting the remote data to obtain the local predictions. The data were also high-pass filtered using a four-pole Butterworth filter with a corner frequency of 10^{-4} Hz prior to Fourier transformation into the frequency domain, to best match the frequency bandwidth of the MT transfer functions typically available for EarthScope MT stations (~10^{-4} Hz – 10^{-1} Hz or 10 s to 10,000 s period).

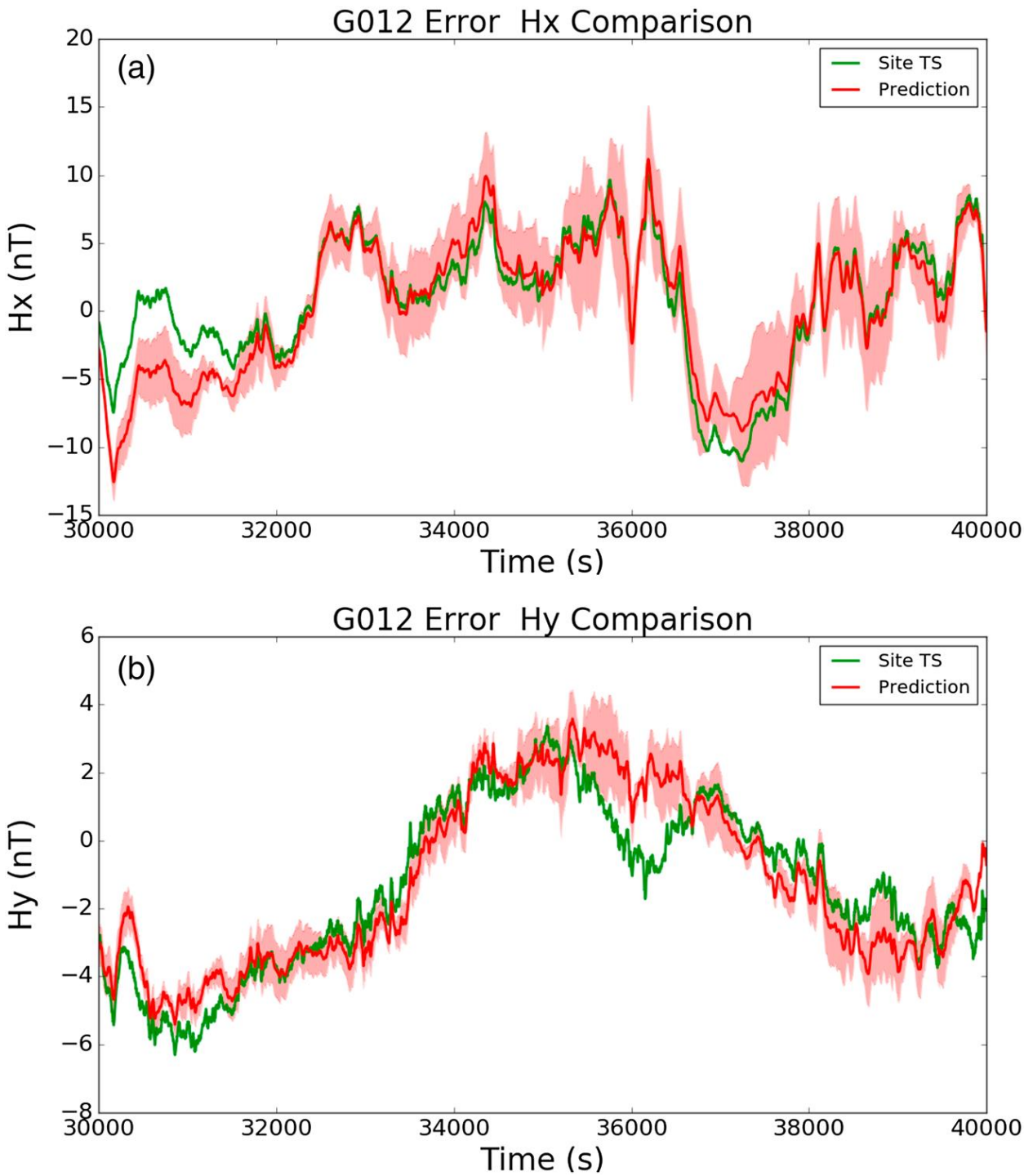

Figure 2.6. High-pass filtered magnetic field time series for data recorded at MT site G012 (green curves) and for data predicted for that location _95% confidence interval (red curves) by projection of vector magnetic field variation data recorded at the four magnetic observatories, projected through a multiple station transfer function, shown in the (a) north-south (x) and (b) east-west (y).

2.4.3 Projections of Local Magnetic Fields Through the MT Impedance Tensor

The final step in the CLFA process of predicting the local electric field variations at each MT station involves projecting the predicted magnetic fields for that location through the local MT impedance tensor. Any deficiencies in the projected magnetic fields at that site (which could contain signal components that are nonstationary and that may be contaminated by non-plane wave sources such as artifacts of cultural noise) through an impedance tensor that may itself contain a degree of error could degrade the fidelity of the resulting predicted electric field.

As a first step, we examine the quality of the electric field prediction that would result from projecting the magnetic fields actually recorded at the MT station through the local impedance tensor. In principle, such a predicted electric field should closely match the recorded field, since the recorded fields were used to estimate the impedance tensor. The purpose of this exercise is to demonstrate what portion of the original signal is not adequately modeled by the impedance tensor, which is a linear filter estimated by assuming the source signal is a stationary plane wave, and that downweighted the influence of data sections that violated that assumption. The result is seen in Figure 2.7.

Figures 2.6 and 2.7 both show high coherence between measured and predicted magnetic and electric field components, respectively, although the smaller uncertainty in the predicted electric fields in Figure 2.7 relative to the uncertainty in the predicted magnetic fields in Figure 2.6 reflects the larger uncertainty in the multiple station magnetic field transfer function relative to the uncertainty in the local impedance tensor estimate. This likely reflects more complex noise structures and lower coherences between magnetic fields at sites separated by many hundreds-to-thousands of kilometers relative to the purely local electric and magnetic field relationships at the magnetotelluric station. Aside from some long-period drift and scaling issues that are occasionally present in the field predictions, the multiple station transfer function-based prediction filter and the local impedance tensor prediction filter are demonstrated to adequately replicate the measured data at the MT sites within the frequency range for which the impedance tensor is known.

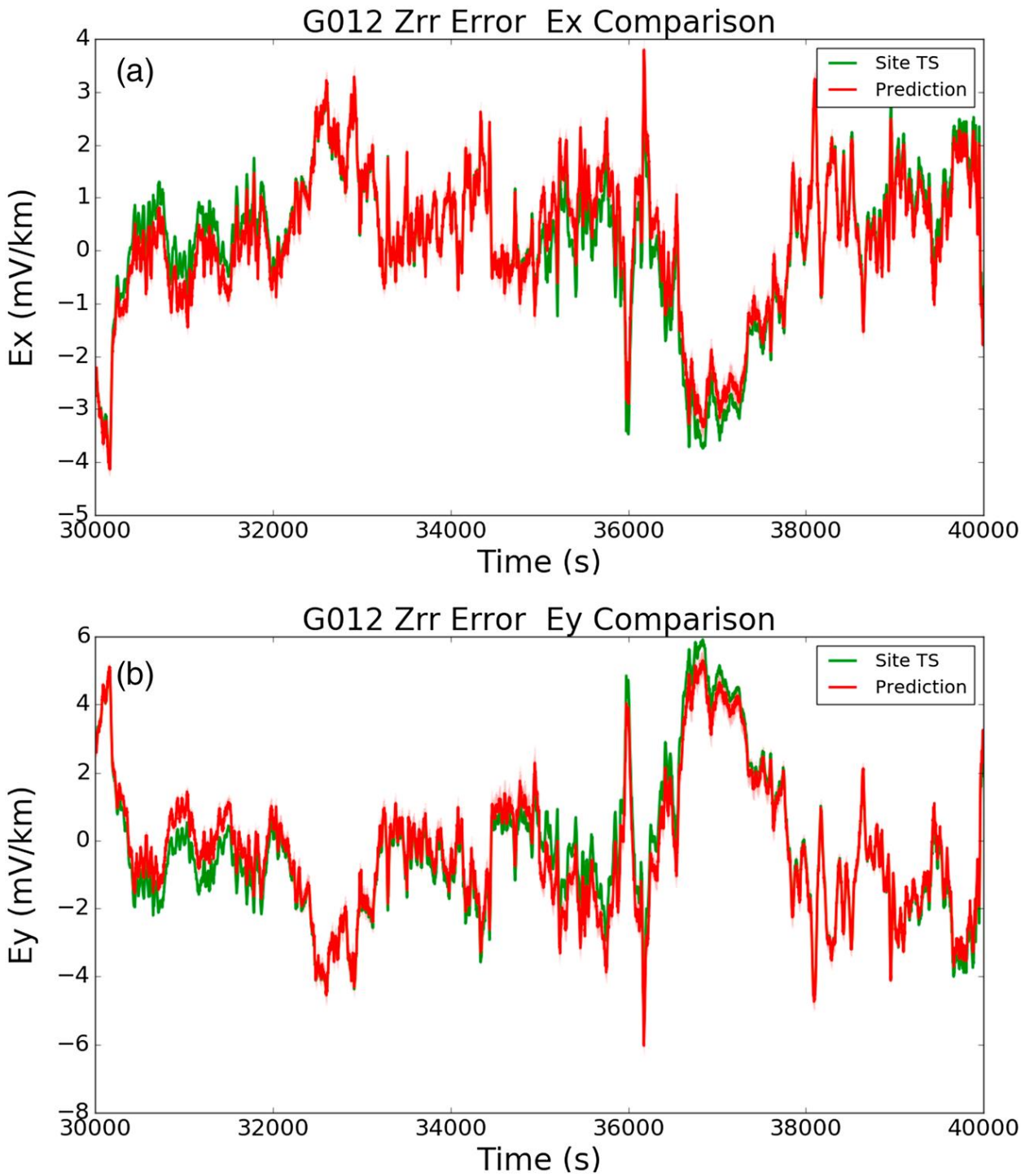

Figure 2.7. High-pass filtered electric field time series for data recorded at MT site G012 (green curves) and for data predicted for that location ±95% confidence interval (red curves) by projecting the locally recorded magnetic field data at that site through the local impedance tensor to yield the prediction of the local electric field at that site. Two sets of orthogonal electric field components are shown in the (a) north-south (x) and (b) east-west (y) directions.

2.4.4 Projections of Predicted Magnetic Fields Through the MT Impedance Tensor

Projecting the magnetic field at the four remote magnetic observatories through the multistation transfer function and then projecting the resulting predicted magnetic field at the MT station through the local impedance tensor leads to the electric field predictions shown in Figure 2.8. This series of steps constitutes the full CLFA prediction process. These results can be contrasted with Figure 2.7 to gauge the impact of projecting predicted versus actual magnetic fields through the impedance tensor. The predicted electric field components at the MT site retains high coherence with the electric field components actually recorded at the site despite the minor compounding misfit introduced from the magnetic and electric portions of the prediction process that were shown previously, of which the propagated uncertainty in the magnetic field prediction is the dominant contributor. Misfits appear to scale with the magnitude of the signal, which is demonstrated most clearly in the Ey prediction. Overall, we found that our prediction algorithm produces low electric field prediction misfits at most sites that are typically around 1–2 mV/km RMS, aside from the occasional outlying peak or interludes of reduced coherence that appear as phase shifts or noise. High coherence and low misfit are retained for the great majority of 10,000s time series sections at multiple MT sites that we have examined.

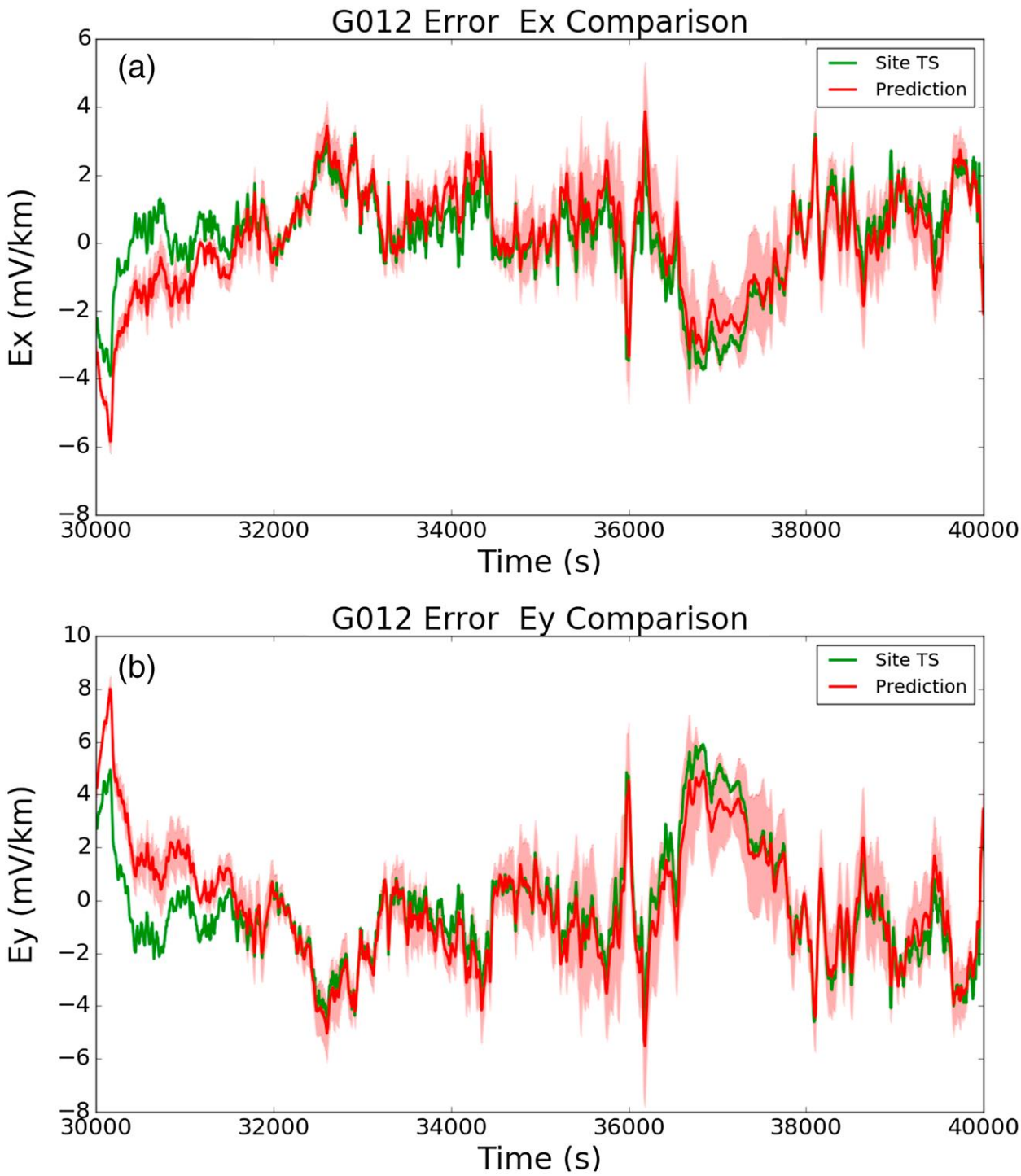

Figure 2.8. High-pass filtered electric field time series for data recorded at MT site G012 (green curves) and for data predicted for that location _95% confidence interval (red curves) by projecting the vector magnetic field variation data recorded at the four magnetic observatories through a multiple station transfer function, resulting in a predicted magnetic field that is then projected through the local impedance tensor to yield the prediction of the local electric field at that site. Two sets of orthogonal electric field components are shown in the (a) north-south (x) and (b) east-west (y) directions.

2.4.5 Nearest Neighbor Interpolation of Ground Electric Fields

In section 2.3.1 above, we described our algorithm for distance-weighted interpolation of the predicted ground electric field vector components from a set of MT stations that most immediately surround a given point along the path of a power transmission line. While in the present work we can provide no examples within our MT station array of electric fields as actually measured along a transmission line, we illustrate the effectiveness of this interpolation method by carrying out a Delaunay triangulation of our MT array (Figure 2.2) with a single-station location deleted and then interpolating on to the location of that missing station the electric fields predicted using the CLFA method from the three MT station locations most closely surrounding it. We compare these interpolated electric field components with the CLFA prediction of the electric field calculated for that site.

For this purpose, we require a set of three MT stations that form a Delaunay triangle that encloses a fourth station, all of which recorded electric fields simultaneously for a considerable period of time. The station combination C013, C015, and D013 (Figure 2.2) met this condition and serves as the vertices of the enclosing Delaunay triangle around station C014. (The Delaunay triangles shown in Figure 2.2 are for the complete set of all MT stations in the array and do not show the new Delaunay triangle that connects stations C013, C015, and D013 once station C014 is omitted from the array.) Figure 2.9 shows the result of the nearest neighbor electric field interpolation for a time series section, displayed on a fine scale of ~1 day time duration and over a ±3 mV/km range. As indicated previously it is still an open question whether local electric field distortion at each site will inevitably degrade the fidelity of the geographically interpolated fields, introducing potentially larger errors than alternative approaches based on the forward solution for the electric fields above a model of known conductivity. In the present example, where the distance between local station C014 and the interpolating stations ranges between 11 km and 16 km, and all sites lie within a similar geologic setting, nearest neighbor interpolation of the predicted electric fields matches the site prediction of the electric fields to within a fraction of a mV/km aside from brief excursions of O(1 mV/km) specifically in the Ex component. This discrepancy is smaller than the typical misfit between predicted and measured electric fields reported earlier (Figure 2.8) so lies within the margin of error.

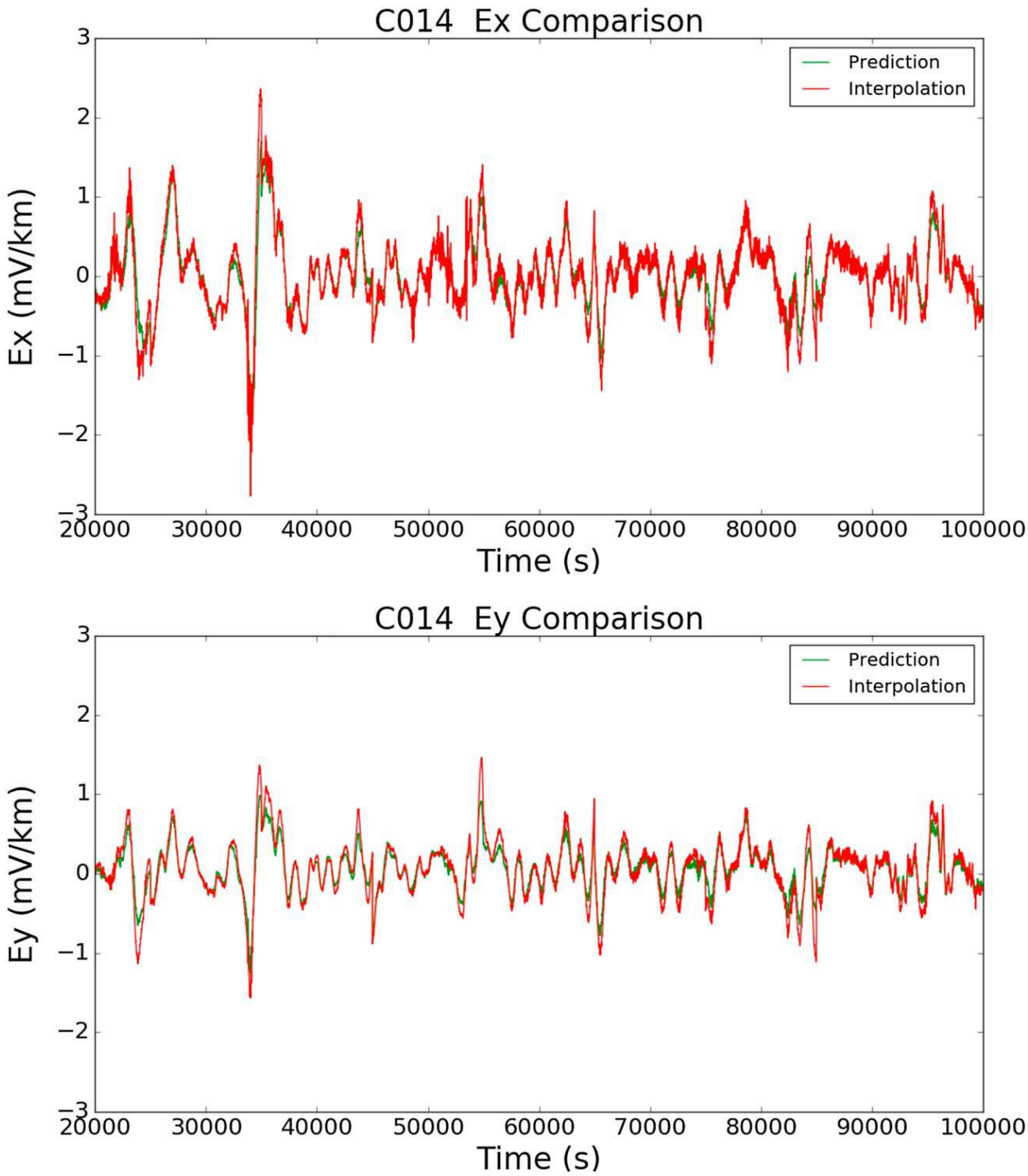

Figure 2.9. CLFA prediction of the (top) north-south (Ex) and (bottom) east-west (Ey) electric field components at MT station C014 (red curves) and nearest neighbor interpolation by distance-weighted averaging of the CLFA predictions of these same components from MT stations C013, C015, and D013 (see Figure 2.2 for station locations).

The example shown above where the distance from the interpolating point to the most distant MT station does not exceed 16 km reflects the augmentation of the EarthScope MT Transportable Array, with nominal 70 km MT station spacing (Figure 2.1), with a much finer station spacing of the EarthScope-GeoPRISMS special study area MT array in western Oregon and southwestern Washington (Figure 2.2). More typically, where EarthScope MT data exist, it is on the ~70 km station spacing grid seen in Figure 2.1, which could lead to a maximum distance from the interpolating point along a power transmission line path and an EarthScope MT station approximately three times greater than the example shown here. We have repeated all steps shown above to predict and project electric fields for a more typical ~70 km EarthScope MT array for a power transmission line in Wisconsin and Michigan. While the results are not shown here (they will be the subject of a subsequent paper), we can report that the degradation in fidelity of the interpolated electric fields is very modest and within the confidence limits of the predicted electric fields at the MT station locations.

2.4.6 Comparing our Results to Those Generated From 1-D Conductivity Models

Our CLFA electric field predictions can be compared to those generated by following the North American Electric Reliability Corporation (NERC) guidelines outlined in North American Electric Reliability Corporation (NERC) [2013]. Rather than constructing a series of cascading linear filters as we have done to project the magnetic fields measured at multiple magnetic observatories to the location of interest and then projecting the resulting predicted magnetic field through the local MT impedance tensor, the NERC guidelines directly employ the magnetic field data from the nearest USGS magnetic observatory as representative of the magnetic field at the local site. The NERC guidelines then call for solving the electromagnetic induction problem for the predicted electric fields above a known 1-D Earth conductivity profile, given the magnetic observatory magnetic field data as input. There do not appear to be any set NERC standards for specific window type, window length, filtering level, or various other parameters, so the same values that we used with our method were used for consistency. We solved for the 1-D impedance at the same set of frequencies at which EarthScope 3-D impedances are calculated, but for the 1-D electrical conductivity model found in the EPRI [2002] PB-1 conductivity map that represents the area containing our MT array.

Figure 2.10 displays a direct comparison at MT station G012 (see Figure 2.2) between the NERC electric field time series predictions, our CLFA based predictions, the original time series, and a hybrid method where our (linear filter) predicted magnetic field was instead projected through the EPRI [2002] 1-D model impedance rather than through the (3-D) EarthScope impedance tensor for that site. By presenting the results of the hybrid method in comparison to the CLFA results, we eliminate any variation due to differences in the magnetic fields used for the calculation and instead illuminate the differences attributable solely to using 1-D versus 3-D ground conductivity information. Figure 2.10 also displays a comparison between these various predictions but for a much longer time period, which is displayed as RMS misfit between the recorded and predicted electric fields, binned into 6 h intervals.

The first thing to note is that our linear filter prediction method generates values that better match the electric field time series that were actually recorded at the MT stations, with lower misfit across all timescales (Figures 2.10 and 2.11). While we show examples from MT station G012, this statement is true at all stations that we have examined within the MT array shown in Figure 2.2. This difference is more clearly demonstrated in Ex than in Ey at MT site G012, which can be explained by the strongly 2-D nature of the electric conductivity structure beneath that location. For 2-D electrical structure, the impedance tensor can be rotated into the direction of geoelectric strike, where impedance tensor element $Z_{x'y'}$ (equation (2.1)) represents the transverse electric (TE) mode where the electric field is parallel to strike and $Z_{y'x'}$ represents transverse magnetic (TM) mode where the electric field is perpendicular to strike. The primed subscripts refer to the rotated coordinates, where x' is aligned with strike direction. TE and TM mode impedances exhibit different sensitivity to the presence of higher dimensional structure. For the present example, the Ex component of the predicted field is highly sensitive to the presence of 2-D and higher dimensional ground electrical structure, whereas the Ey component is less so. As a consequence of this, the electric field prediction based on the NERC guidelines does a particularly poor job of fitting the Ex electric field that was actually recorded at site G012. The short timescale NERC guideline-based predictions of Ey match the high-frequency variations in the Ey time series recorded at the site (Figure 2.10), but there are significant peaks, troughs, and longer period changes that are completely missed in the predicted Ex component.

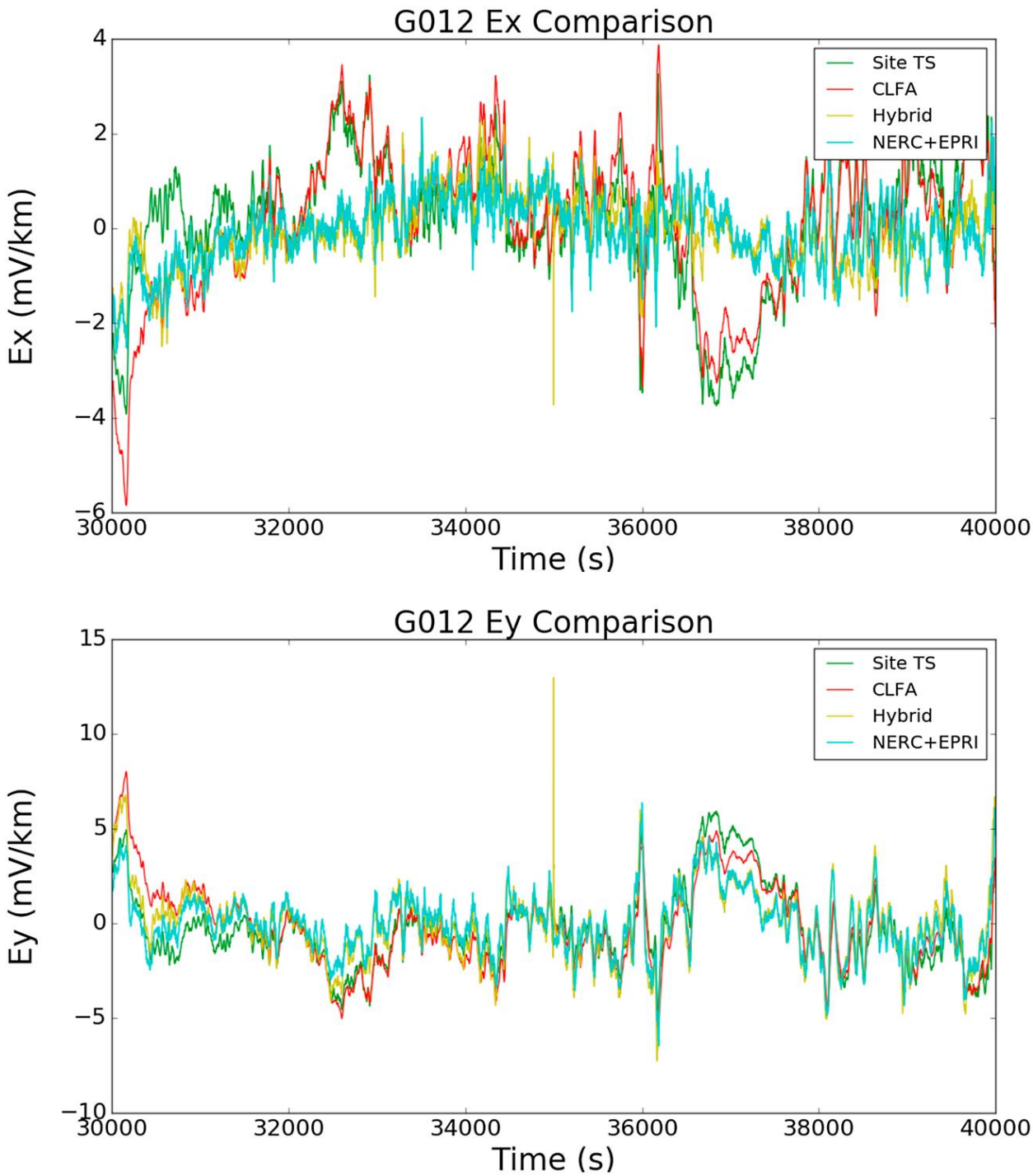

Figure 2.10. High-pass filtered electric field time series for data recorded at MT site G012 (green curves) and for electric field data predicted for that location using NERC (cyan curves), hybrid (yellow curves), and our cascading linear filter algorithm (red curves), in the (top) north-south (x) and (bottom) east-west (y) directions for a 10,000 s time series section.

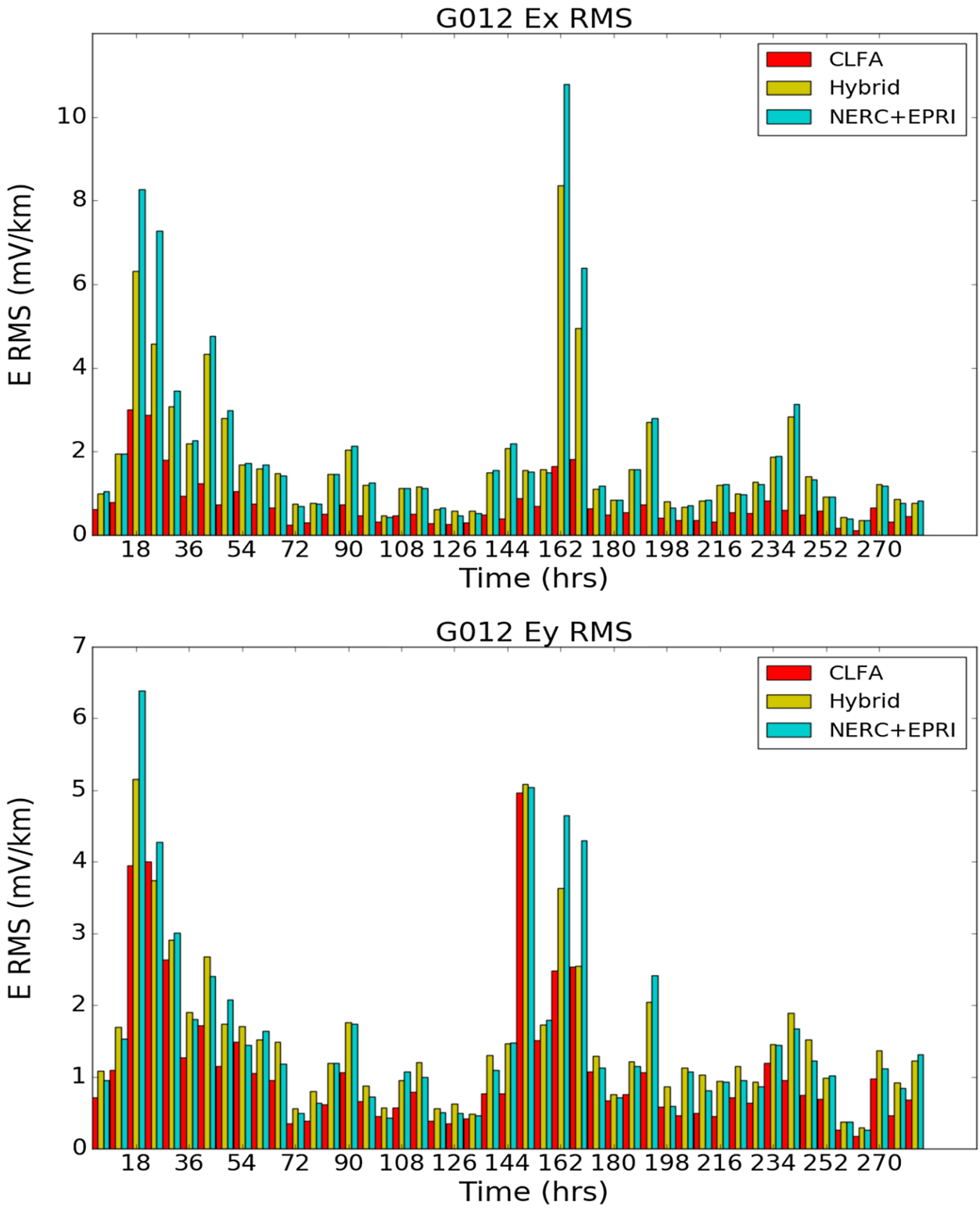

Figure 2.11. RMS misfit between the (top) north-south (Ex) and (bottom) east-west (Ey) electric field components actually measured at MT station location G012 and those predicted by the NERC (cyan), hybrid (yellow), and the CLFA (red) methods, calculated within 6 h bins for a 106 s time series section.

The quality of predictions for both Ex and Ey obtained following NERC guidelines would likely degrade more severely in the presence of highly 3-D conductive structures, since there would be no preferred geoelectric strike direction, and higher dimensional effects would be seen strongly in both electric field components. This is also the case for predictions based on the hybrid method. In both cases we have found that the impact of higher dimensional ground conductivity structure on the degradation of ground electric field predictions is the dominant source of error in the predictions, rather than the modest differences in the quality of the predicted magnetic field. Our proposed CLFA linear filter prediction method accommodates higher dimensional ground conductivity structure implicitly and is better able to match the electric field data actually recorded at the MT stations.

The same trends over the 10,000 s time series section displayed in Figure 2.10 are also observed for time series sections up to and including 106 s long (the longest section we have examined). Since it is difficult to clearly display such a large number of points to visualize the details of the misfit, over each interval of 6 h, we have calculated the RMS misfit between the measured electric field components at MT site G012 and the predicted electric fields at that site according to

$$RMS = \sqrt{\frac{1}{n}\sum_{i=1}^{n}(site_i - pred_i)^2} \ , \tag{2.6}$$

where $site_i$ is the measured field and $pred_i$ is the predicted field. This is seen for a 10^6 s time series section in Figure 2.11.

As would be expected from the previous comparisons, the RMS misfit between recorded and predicted electric fields is fairly similar for the Ey component from all three prediction methods, whereas for the Ex component (which is more influenced by non-1-D electrical conductivity structure than Ey in this case), our cascading linear filter algorithm has much lower RMS misfit than either the NERC method or the hybrid method. In particular, electric field predictions from the NERC method can misfit the electric fields actually recorded at the MT station locations by several hundreds of percent more than those calculated using the CLFA approach. This is evidence that methods that employ 1-D ground conductivity models have noticeable limitations on accuracy outside of those atypical locations where ground conductivity structure is approximately 1-D.

One of the rationales for applying the NERC guidelines, which employ 1-D models of ground conductivity rather than the more complex data-based 3-D impedances used in the CLFA approach, is that 1-D methods are still capable of reliably estimating peaks in GMD-induced ground electric field intensity that would actually cause or indicate GIC events, so the degree of mismatch on smaller fluctuations is unimportant. Figure 2.11 demonstrates that this reasoning is questionable for locations with heterogeneous (2-D or 3-D) electrical structure. The EarthScope MT program has revealed that highly 3-D structure is ubiquitous throughout all regions that have been instrumented (Figure 2.1), which currently comprises nearly half of the territory of the continental U.S. (including the Pacific Northwest area that serves as our test bed for this paper). It is premature to conclude anything about the effects of these discrepancies on predicting actual GIC events, particularly since the act of integrating ground electric fields along power line paths could reduce the impact of 3-D variations, at least for certain geographic settings and power distribution topologies, yet it does seem clear that by disregarding the 3-D information contained in MT impedance tensors and basing ground electric field predictions on 1-D models, significant inaccuracies can result.

2.5 Discussion

The main limitation apparent from these examples is the need to use a high-pass filtered version of the site time series to assess fit since long-period signals outside of the frequency band for which the impedance tensor is known (such as diurnal variations in the electric and magnetic fields) would otherwise leak energy into the frequency bands of interest, thereby introducing long-term drift that could degrade the predictions. One method of resolving this issue would be to extend the MT impedance tensors to lower frequencies in order to capture diurnal variations. This is problematic, since for the case of EarthScope and similar temporary campaign-style MT investigations, the finite duration of the data set limits the lowest frequencies to the values already achieved. While there are a limited number of EarthScope MT stations that were specifically designed to obtain MT impedance data to frequencies as low as 10^{-5} Hz, it is technically very challenging to obtain stable electric field measurement at such low frequencies, so these were exceptional installations and do not provide a general solution to this issue. Another approach is to make use of deeper, global-scale 3-D mantle conductivity models that

have been obtained through methods involving analyses of magnetic field data exclusively [Kelbert et al., 2009; Sun et al., 2015]. While having effectively no spatial resolving power in the upper ~350 km of the crust and mantle, these models typically describe deep Earth conductivity variations for mantle depths of ~350 km–~1200 km in terms of an underlying radially symmetric (i.e., 1-D model) compromising a series of radial shells of finite thickness, with 3-D variations in conductivity represented as a set of spherical harmonic coefficients about the underlying baseline model. By solving the forward problem for 3-D induction for such a model, a set of equivalent MT impedance functions could be generated at the MT station locations to provide the lower frequencies that otherwise are absent from the EarthScope impedance tensors. By appending these ultralow frequency impedances to the MT impedances, this could provide predictions free from the minor long-period drift issues we sometime encounter, which would generate even closer real-time total electric field predictions and thus improve GIC mitigation.

The cascading linear filter algorithm (CLFA) we have demonstrated, making use of 3-D information implicit in the impedance tensors, reproduces ground electric fields with greater fidelity than the NERC guidelines approach or the hybrid approach, and its computational demands are very modest. To gauge the suitability of the CLFA code for operation in industrial settings with modest computing infrastructure, we have tested the algorithm on an obsolete desktop computer with an Intel® Celeron® G1610 (2.6 0GHz) processor, 4 GB of DDR3 SRAM, under the MS Windows 8™ 64-bit operating system, and find that predicting electric field values given a 100,000 s section of magnetic observatory data takes ~1 s to run on such a computer. Minor efficiency improvements and parallelization of series components of the code, or simply running it on a faster computer would speed computations to a fraction of a second, enabling true real-time ground electric field calculations. Internet latency and throughput can be a consideration in maintaining real-time electric field prediction capabilities. In our experience there is a 10–15 s latency between requesting data from the USGS servers and receiving it through the Internet regardless of the length of the data set requested, even when using hard-wired internet connections that otherwise are able to maintain gigabit per second speeds to distant servers.

While a delay of up to 15 s might not pose a serious problem for operational GIC prediction, in the event true real time throughput is needed, a small array of observatory quality

magnetometers could be installed at sites close to the power grid to transmit data through dedicated telemetry links. In addition to reducing the latency of obtaining magnetic field data, the fidelity of the electric field predictions along the power line path would likely improve given the decreased distances involved. Nearby magnetometers could also provide estimates for local noise, which is important to the electric field but neglected at present.

Combining all of the suggestions would likely further improve ground electric field predictions, GIC mitigation, and power grid safety, yet the current estimates based solely on distant magnetic observatory data still appear to be useful even without further improvement. This bodes well for integrating the output of our real-time algorithm and its output of nonuniform electric fields as the input into industrial GIC prediction software. The next step in this research effort is to carry out such integration with industrial GIC prediction software, which we plan to do after we complete additional improvements to long-period ground electric field predictions.

2.6 Conclusions

A new cascading linear filter algorithm (CLFA) for accurately predicting the horizontal vector components of ground electric fields in real time, needed for predictions of geomagnetically induced currents (GICs), was described, tested for numerical and methodological validity, and examined for potential issues or improvements. The CLFA method projects the horizontal vector components of the magnetic field variations at a set of magnetic observatories through a multiple station transfer function (the first CLFA linear filter) to generate a predicted local magnetic field time series at each of a set of locations where magnetotelluric impedance tensors had been previously obtained. The predicted magnetic fields are then projected through the impedance tensors (the second CLFA linear filter) to predict the horizontal vector components of the ground electric fields at those locations. In the final step, a nearest neighbor interpolation algorithm is used to project the predicted electric fields onto the path of power lines that lie within the footprint of the magnetotelluric sites. The CLFA method was found to run sufficiently fast to enable real-time prediction throughput to be achieved, barring solvable data acquisition difficulties, and was shown to produce predictions of high coherence and low misfit with the time series that were predicted. Improvements in the fidelity of the

predicted electric fields may result from appending lower frequency impedance estimates from global scale electrical conductivity models of the mid-to-lower mantle to the MT-derived impedance tensors to more faithfully capture long-period (e.g., diurnal) variations in the electric field. Despite existing limitations, the CLFA ground electric field yielded significantly lower misfits to electric field data actually measured at the MT sites than predictions made using either NERC [2013] guidelines or a proposed hybrid method. We attribute this to the CLFA method's incorporation of 3-D ground conductivity information through the use of the full MT impedance tensors, rather than reliance of older regional 1-D models of ground conductivity that have been shown not to reflect the true complexity of the electric structure of the crust and mantle.

3. Comparison of rapid electric field prediction algorithms and related geomagnetically induced current estimates for test cases in regions of three-dimensional ground conductivity

Abstract

Geomagnetically induced currents (GICs) within a power system are calculated from ground level electric field predictions, which are currently produced using an industry standard practice that is based on regional 1-D ground electrical conductivity. Ground conductivity can vary by at least three orders of magnitude in all three dimensions, so electric field predictions that employ solutions to the governing equations for a 1-D ground conductivity model may deviate significantly from actual ground fields. A 3-D magnetotelluric (MT) based algorithm, that still retains the computational speed and lightness of the 1-D method, is proposed, and GIC predictions resulting from the potentially differing techniques are compared for multiple test cases within the NSF EarthScope MT Transportable Array. Electric field amplification and vector orientation for sites within the array are also compared with the resulting GIC predictions and used as general identification techniques for areas that are prone to GIC effects. Two powerline test cases of varying geometry, and a large equivalent circuit that serves as a model for a canonical power grid, are examined to determine if 3-D electric field effects average out over large distances, as previously claimed, or if discrepancies between the models affect the reliability of existing power infrastructure.

3.1 Introduction

Geomagnetically Induced Currents (GICs) are quasi-DC signals that are induced from large fluctuations in the Earth's electric and magnetic fields. Such fluctuations, called Geomagnetic Disturbances (GMDs), are mainly dictated by the interplay between solar wind and the Earth's magnetosphere. Major factors that alter this interplay include the 11-year sunspot cycle, Coronal Mass Ejections (CMEs), and the magnetic field coupling between planetary bodies. These factors often have cyclical patterns that are capable of constructively reinforcing or acting chaotically, which cause GICs to be a complex and continual threat. Regarding the power industry, GIC events are capable of producing currents strong enough to enter the grounding of transformers, where they then flow through the windings and produce a magnetic field capable of saturating the core [Molinski, 2002]. This half-cycle saturation can alter the AC

waveform of transmitted power and lead to system relay interference, reactive power loss, voltage collapse, and transformer failure depending on the strength of the currents and the protective systems in place [Molinski, 2002; Pirjola *et al*., 2000b]. These negative effects, and the GICs that cause them, are also affected by location in addition to time-dependent space weather factors. The main spatial components that amplify GICs are high geomagnetic latitudes, where large electromagnetic events such as auroral excitations and electrojet currents predominantly occur [Ngwira *et al*., 2013], and areas with higher electrical resistivity ground (crust and mantle) materials such as continental shields [Cherevatova, 2015] that usually intensify ground electric fields. CMEs and other interplanetary events are capable of driving GIC events outside of these regions [Kataoka and Pulkkinen, 2008], and peak amplification can occur even within approximately uniform regional fields during severe GMDs [Pulkkinen *et al*, 2015; Ngwira *et al.*, 2015], so the threat of strong GICs is widespread, with specific locations posing increased risk.

US power utilities currently employ a computationally fast and light GIC prediction method that projects magnetic time series data from the closest United States Geological Survey (USGS) magnetic observatory through a 1-Dimensional impedance that is representative of the physiographic region, which has values that vary with depth and are derived from an EPRI report [Electric Power Research Institute (EPRI), 2002; Pulkkinen *et al.*, 2007]. The North American Energy Reliability Corporation (NERC) has published white papers that detail this technique [NERC, 2013; NERC, 2016] so the method will be referred to as the NERC method for the rest of the paper. The NERC method predicts that all points within the same physiographic province will have the same uniform electric field, yet a variety of recent magnetotelluric (MT) studies [Kelbert *et al*., 2012; Meqbel *et al*., 2014; Schultz *et al*., 2014; Evans *et al*., 2014] have indicated that electrical conductivity in the crust and mantle can vary in all three spatial dimensions, with more than three orders-of-magnitude difference at several locations, depths, and spatial scales. These 3-Dimensional conductivity variations can cause large ground electric field amplification [Thomson *et al.*, 2005; Bedrosian and Love, 2015; Love *et al*., 2016], and do not reflect the regional structure presented in the 1-D model. This mismatch suggests that the NERC method can produce electric field predictions that greatly under or over estimate the actual electric field values, and resulting GIC effects, in conductively heterogeneous areas such as the Pacific Northwest region of the United States. It is argued that integration of the ground electric field

along a power transmission system to obtain GIC predictions averages out 3-D effects, though this claim is refuted by the work of Burstinghaus *et al.* [2013] and will be tested in the results section. Our previous work [Bonner & Schultz, 2017] has suggested that the downside of increased computational cost for 3-D accuracy, which is shown in multiple recent studies [Love and Swindinsky,2014; Vanhamaki *et al.*,2009; De Villiers and Cilliers, 2014; Simpson, 2009], can be counteracted by using magnetotelluric (MT) data products, so the next step is to test if our proposed method can produce more accurate GIC predictions rapidly enough to be of use to the power industry.

3.1.1 The Cascading Linear Filter Algorithm (CLFA) Method and Tested Region

For a comprehensive explanation of the CLFA data flow process, its limitations, and the theoretical background that supports it, we refer the reader to our previous paper that originally proposed the method [Bonner and Schultz, 2017]. This work utilizes an amended version of the same technique that interpolates the predicted site electric fields onto equally spaced points that comprise a grid, which contains the tested powerline or circuit, instead of interpolating the electric fields onto points that represent the tested system directly. The interpolation scheme was changed to enable the electric field predictions to be read into power flow simulation software, which will be explained in section 3.1.2. The updated data flow is shown below in Fig. 3.1.

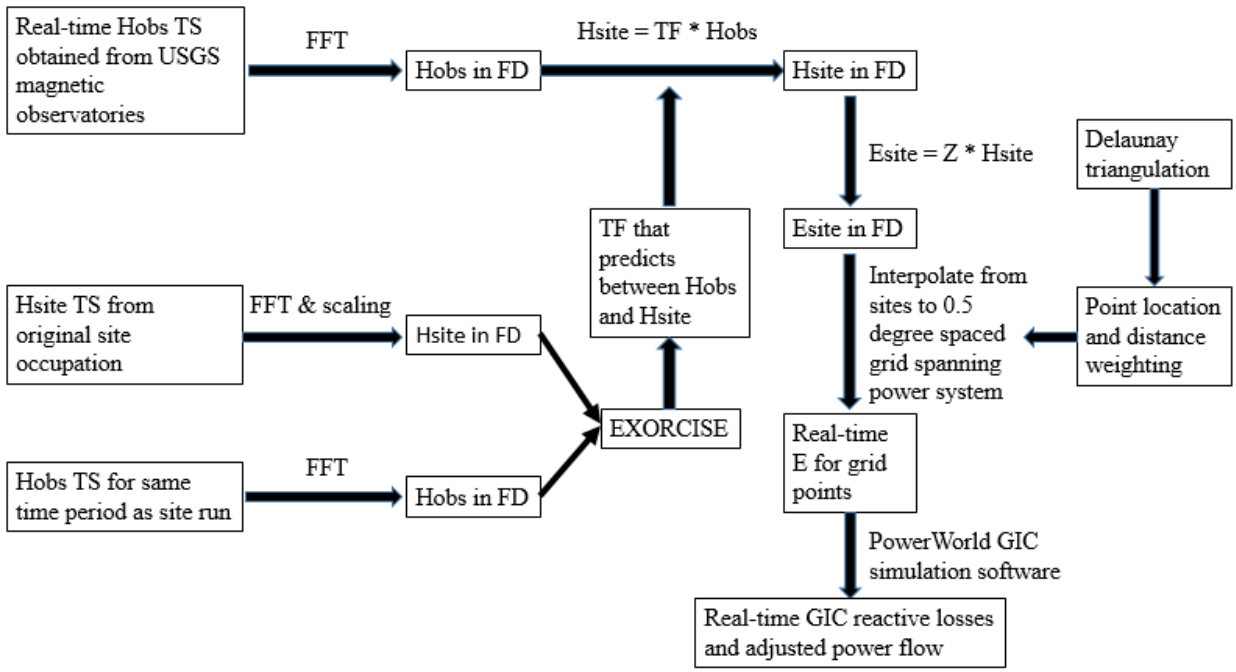

Figure 3.1: Data flow chart of CLFA method, where TF stands for transfer function, TS represents time series, FD indicates the frequency domain, and FFT corresponds to fast Fourier transformation

The MT data used in this study comprise the western portion of the NSF-funded EarthScope Transportable Array and the entirety of the NSF-funded joint EarthScope-GeoPRISMS project EAR-1053632, "Onshore-offshore MT Investigation of Cascadia Margin 3-D Structure, Segmentation and Fluid Distribution,", which will be referred to as MOCHA for this paper. The western EarthScope array contained a set of temporary MT stations with 70 km nominal spacing that spanned from Washington to northern California by latitude and Washington to Montana by longitude [Schultz, 2009], while the MOCHA array had 20 km nominal spacing and covered southwestern Washington and western Oregon. The MOCHA array was tested in the previous paper, and the EarthScope Transportable array section was added to the array used in this paper to allow for larger test cases to be analyzed. Both arrays are shown in Fig. 3.2, along with the Delaunay triangulation based interpolation scheme that combines them into a single system.

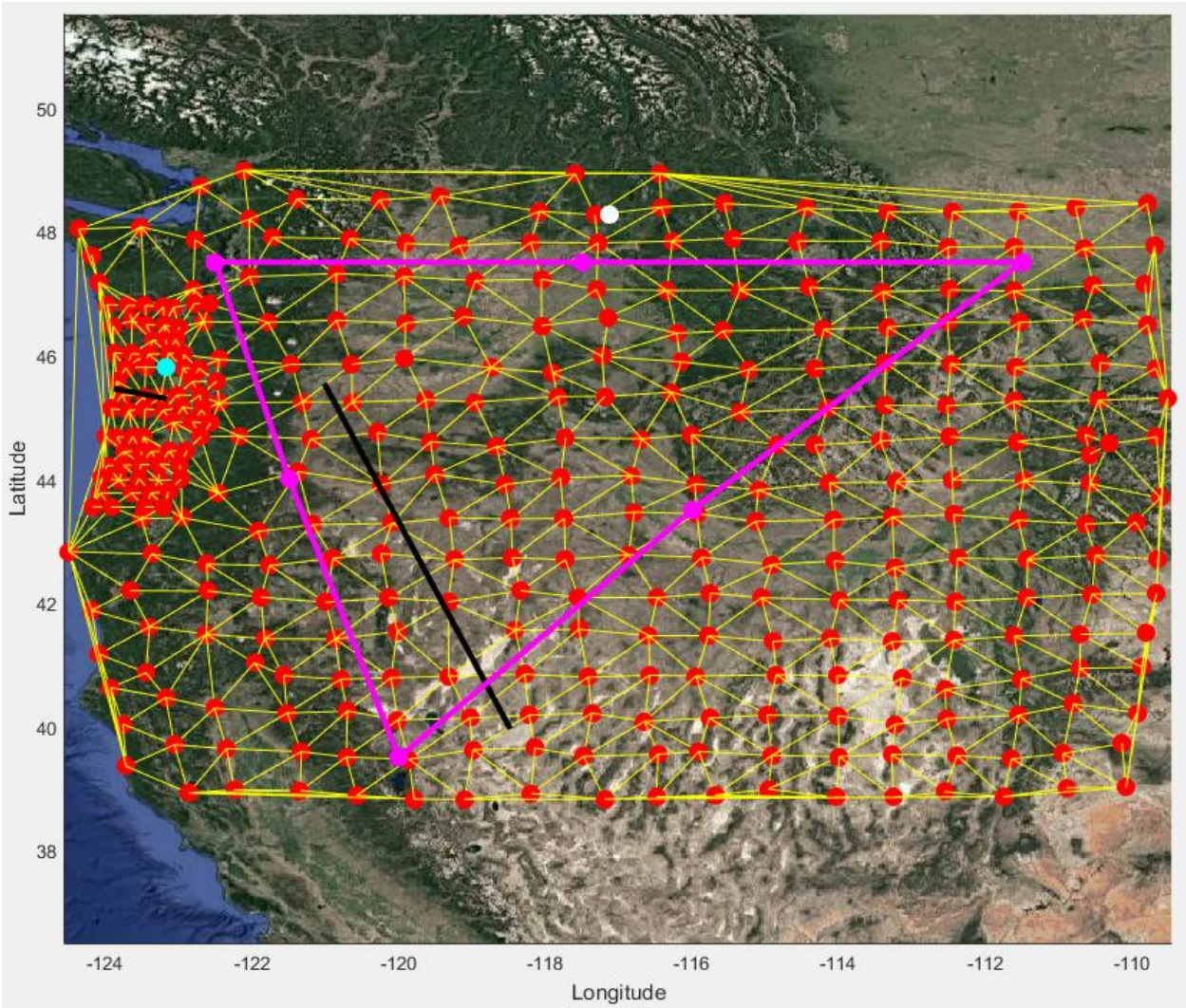

Figure 3.2: Map of the Delaunay triangulation formed by combining the western portion of the EarthScope Transportable Magnetotelluric Array and MOCHA MT array. MT sites are shown in red, triangulation bounds or edges in yellow, site G012 that is used for later comparisons in blue, the Tillamook-Carlton transmission line in the western black line, the Pacific DC Intertie test line in the eastern black line, points and lines representing the WECC test circuit in purple, and the Newport magnetic (NEW) in white. The MOCHA sites are shown by the higher density site cluster in southwestern Washington and western Oregon.

3.1.2 GIC Prediction Software and Test Cases

GIC predictions are obtained by implementing the interpolated CLFA-based electric field predictions into a power flow simulator that calculates the reactive power loss and power flow solution for the tested system. PowerWorld™ [Overbye *et al.*, 1995; PowerWorld 2011] and Siemens' PSS®E [Siemens Energy, 2016] are examples of power flow simulation programs,

which calculate various values for the user provided circuit and situation. Users input a one-line circuit diagram, with set parameters such as voltage and resistance, that represents the tested situation and can then alter the system, through setting a fault on one of the lines for example, to predict how the system would react. Power flow solutions are obtained through an iterative optimization process, such as the Gauss-Seidel or Newton-Raphson methods [Glover *et al.*, 2012], to generate these system predictions. For GICs, the main parameters that are useful for testing are reactive power loss, GIC voltage, and GIC current. Reactive power is the imaginary component of power and it does not flow or provide any work to the system, though it is vital for maintaining voltage levels. High reactive power loss is associated with voltage collapse and blackouts, so it serves as a useful indicator for the overall impact of GIC effects for a portion or the entirety of the tested system.

GIC prediction software, such as the GIC packages found in PowerWorld™ and PSS®E, begins the prediction process by determining the conductivity matrix that represents the provided system. The conductivity matrix is *n x n* for an n bus system and the entries are given by the conductance between buses *i* and *k* for matrix element G_{ik}, with conductance relating to the sum of all provided transmission line resistances connected to each bus. Next, the electric fields along each transmission line are integrated into GIC voltages through multiplying the distance between connected power buses by the electric field along that respective line. The electric field is split into North-South (*Ex*) and East-West (*Ey*) components, so this multiplication occurs in parts, with the total GIC voltage equaling the sum of the North-South distance multiplied by *Ex* and the East-West distance multiplied by *Ey* [Horton et al., 2012]. If the fields are uniform then the total distance is multiplied by a constant electric field, typically 1 V/km magnitude with varying levels of rotation for worst-case scenario testing, to obtain a constant GIC line voltage. In our case, the electric field is non-uniform, so the system must be discretized into parts that the electric field is then interpolated on to and summed to obtain time-varying GIC voltages on each line. Each line GIC voltage is then converted into a Norton current for the connected bus based on coil winding properties and grounding resistance of the transformers connected at the bus [Overbye *et al*., 2013]. The conductance matrix *G* and Norton current matrix I_{GIC} can then be combined to obtain the GIC related bus voltage V_{GIC} through

$$V_{GIC} = G^{-1} * I_{GIC} \tag{3.1}$$

This GIC related voltage injection can then be treated as a normal power flow situation and solved using the nodal admittance matrix method and typical power solving techniques [Boteler, 2014; Pirjola, 2002]. Reactive power loss Q_{loss} can also be calculated via

$$Q_{loss} = V_{kV} * k * I_{GIC} \tag{3.2}$$

where V_{kV} is the terminal voltage matrix and k is a transformer constant. [Birchfield *et al*., 2017]. Power system operators or automated response systems can utilize the GIC altered power flows and related reactive power losses to determine actions to minimize damage. When significant power losses or damage to systems are predicted to occur from GIC effects, power can be rerouted through less affected areas like how faults are counteracted, or the grounding circuits in affected transformers can be blocked to prevent GICs from entering the system [Zhu *et al.*, 2014]. Establishing accurate and rapid predictions of GICs within power systems is therefore vital for protecting the power grid.

At the time of this paper, there are no standard GIC test cases, though there are pre-existing test cases that can be given set GIC parameters and placed within the EarthScope MT array for testing. The first power system that will be examined here is the line diagram that is provided with the default GIC module for PowerWorld™ version 19. This line includes two transformers and four buses, with 0.3 Ω coil resistance for the high-side winding of the transformers, 0.2 Ω transformer grounding resistance, and 3 Ω/phase power flow resistance for the transmission line. There are no standard values for these parameters, and they vary greatly by component type and ground material [Overbye *et al*., 2012], so they were kept at the initial values. This line test case was chosen to represent two systems, with one being an East-West oriented line and the other a North-South oriented line. The East-West 230 kV line extends from Tillamook to Carlton, OR and has encountered inaccurately predicted GIC events before [Kappenman & Radasky, 2014]. The North-South line represents the Pacific DC Intertie (Path 65) in the Western Electricity Coordinating Council (WECC) power system, which mainly brings power generated from Oregon's hydroelectric dams in The Dalles, Oregon down to Sylmar, California. Unfortunately, the EarthScope MT array does not extend far enough south to cover the entire line, so the test case line was set to end where the line curves in northwestern Nevada, as can be seen in Fig. 3.2. Path 65 predominantly transports power from north to south,

with a maximum capacity of 3100 MW and voltage of 500 kV [Bonneville Power Administration, 2000], which is reflected in the values set for the one-line diagram of the system. The third test case is a 230 kV 9-bus circuit that was obtained from the Illinois Center for a Smarter Electric Grid website [ICSEG, 2017], which represents a simplification of an old version of the WECC system [AL-Hinai, 2000]. Bus locations were chosen to match major cities within the EarthScope MT array while still fitting the general geometry of the circuit diagram. This decision led to buses 2 and 7 being located at Seattle, WA, bus 8 at Spokane, WA, buses 9 and 3 at Great Falls, MT, bus 5 at Bend, OR, bus 6 at Boise, ID, and buses 4 and 1 at Reno, NV. These locations are shown as purple dots in Fig. 3.2 as well. GIC related parameters for the circuit test case were chosen to be the same as the line case for consistency, though the line resistances were chosen to match the original circuit diagram. The only change that was enacted on all of the test cases involved the transformer GIC response slope, which was set to the first transformer value of 1.067 for every transformer to keep GIC losses consistent at different substations. Both PowerWorld™ and PSS®E were considered for modeling GIC effects, though PSS®E only allows for uniform electric fields [Khosravi and Johansson, 2015], while PowerWorld™ can accept non-uniform field inputs through a file with specified array dimensions and spacing [PowerWorld, 2017]. The power flows and reactive power losses for these two test cases during a variety of input electric fields can be seen in the results section.

3.2 Results

The goal of this work is to advance our previous study [Bonner & Schultz, 2017] by using the Cascading Linear Filter Algorithm (CFLA) to produce electric field predictions for arrays representing several test cases that can be integrated into a power system solver to generate GIC predictions. These GIC predictions can then be compared to predictions obtained from utilizing the industry standard NERC 1-D method to examine the validity and consequences of both approaches. To obtain the CLFA based GIC predictions, we make use of pre-existing electric and magnetic field measurements collected for an array of MT stations that surround the test case locations to calculate observatory-to-site magnetic field transfer functions. These site-based transfer functions allow us to predict the magnetic field for each site in near real-time based on magnetic observatory measurements, and then those site magnetic fields can be projected through the corresponding site impedances to yield electric field predictions. Site

electric field predictions can then be interpolated onto points representing the test case and input into a power solver, such as PowerWorld^{TM}, to generate GIC predictions. We have previously shown that the CLFA method is capable of producing electric field predictions with far lower misfit compared to site measurements than the NERC method in areas of heterogeneous conductivity [Bonner & Schultz, 2017], so we will now test how these differences correspond to variations in GIC predictions for multiple situations and locations.

Throughout this section of the paper, we will examine the conductive structure of the tested region in relation to the resulting electric field predictions and then draw comparisons between the CLFA and NERC based GIC predictions derived from these varying input electric fields. This study first requires an analysis of the level of misfit inherent in both processes to address uncertainty in the subsequent figures and assess the effect of limitations concerning the data sets that were used. Next, electric field amplification contour maps and peak electric field vectors are presented to demonstrate the 3-D conductive features located in the tested region. Then, the magnetic field for a GIC-related spike is shown and compared with the resulting electric field predictions for the CLFA and NERC methods to examine the differences in the output for the two techniques. Lastly, the resulting GIC predictions for the two methods will be analyzed for each of the test cases to characterize differences and consequences of both procedures.

3.2.1 Error Analysis and Data Limitations for Tested Array

We begin our analysis by first addressing a limitation with our data set that prevents full implementation of the CLFA method for the Pacific DC Intertie and WECC circuit test cases. This limitation involves a lack of available 1-second sample rate magnetic observatory data that are concurrent with sites comprising the western portion of the EarthScope magnetotelluric (MT) array. Most of these sites were operated before 2009, when 1-second USGS magnetic observatory data first became available, so observatory time series data near the tested array does not exist to compare with local site measurements. Concurrent observatory and site magnetic time series, sampled at equal time intervals, are required to establish magnetic observatory-to-site transfer functions, which are used to scale near real-time observatory measurements into site magnetic field predictions. Given that magnetic field predictions can therefore not be determined, the measured magnetic field of the nearest observatory is used instead, which is also

done in the NERC method. Spatial variation in the electric field tends to be far greater than in the magnetic field, so the added misfit from using observatory values directly is relatively small, as can be seen in Fig. 3.3. The misfit will thus not invalidate conclusions drawn from results relying on this simplification. Utilizing the same magnetic fields for both the CLFA and NERC methods also restricts variations in the resulting electric field and GIC predictions to the impedance, so the validity of the 3-D vs. 1-D conductivity techniques can be tested directly. The Tillamook – Carlton line is located completely within the MOCHA array, which was operated after 2009, so the full CLFA method can be implemented for that test case to draw comparisons with the partial CFLA cases. The MOCHA data was also collected with a finer spaced grid with higher conductivity resolution, thus resolution in relation to GIC predictions can also be tested.

The relative levels of fit between the concurrent magnetic field time series for the USGS observatories Newport (NEW) and Boulder (BOU), and the MOCHA site G012 are shown below in the top panels of Fig. 3.3. The electric field predictions resulting from projecting the Fourier coefficients of magnetic observatory data through the 3-D site based impedance for G012 are also compared with the measured site electric fields in the middle panels of Fig. 3.3. Comparisons between the misfit for the CLFA and NERC predictions compared to the measured site values are also shown in the bottom panels of Fig. 3.3. Error resulting from uncertainty in the impedance was previously shown to be negligible in comparison to the error in the magnetic field predictions [Bonner & Schultz, 2017], in this case the difference between the chosen observatory and site G012, so Fig. 3.3 serves as a qualitative demonstration of how error involving using observatory magnetic data directly (top panels) corresponds to misfit in the electric field predictions (middle panels). Newport (NEW) was chosen as the closest observatory for all of the tested sites to keep the predictions consistent, and the average distance between NEW and a site within the array is less than the distance to G012 (~500 km), which implies that the average electric field predictions for a site are better than the match between G012 and the predictions from NEW. The low misfit between the measured and NEW predicted electric fields for G012 suggests that the partial CLFA method still produces predictions that are reasonable and valid for analysis. Coherence between the magnetic observatory and MT site time series mainly breaks down from increased distance between the two locations, with latitude differences resulting in greater or lower scaling between the two time series based on the Earth's magnetic field strength and longitude differences causing phase shifts from varied start times in the diurnal

cycle. Boulder is approximately 1500 km away from site G012, which is further than the 1000 km maximum distance between NEW and any of the tested MT sites, though it has a latitude and longitude difference from G012 that is similar to maximum values for the NEW to MT site distances. BOU therefore serves as a good demonstration of the possible effects of latitude and longitude differences, and it also gives an upper bound on the potential misfit for sites within the tested MT array. The CLFA electric field predictions in the bottom panels of Fig. 3.3 also show the level of fit for the MOCHA sites and any other EarthScope MT stations in the United States, barring any significant error in the site impedances or spurious magnetic effects. The bottom panels also compare the level of RMS misfit for the full CLFA and NERC methods, which suggest that the CLFA technique produces more accurate predictions in this region. Misfit is binned into 6 hour intervals and a hybrid method of implementing magnetic field predictions into the NERC 1-D impedance is also included to show the effect of differing impedances.

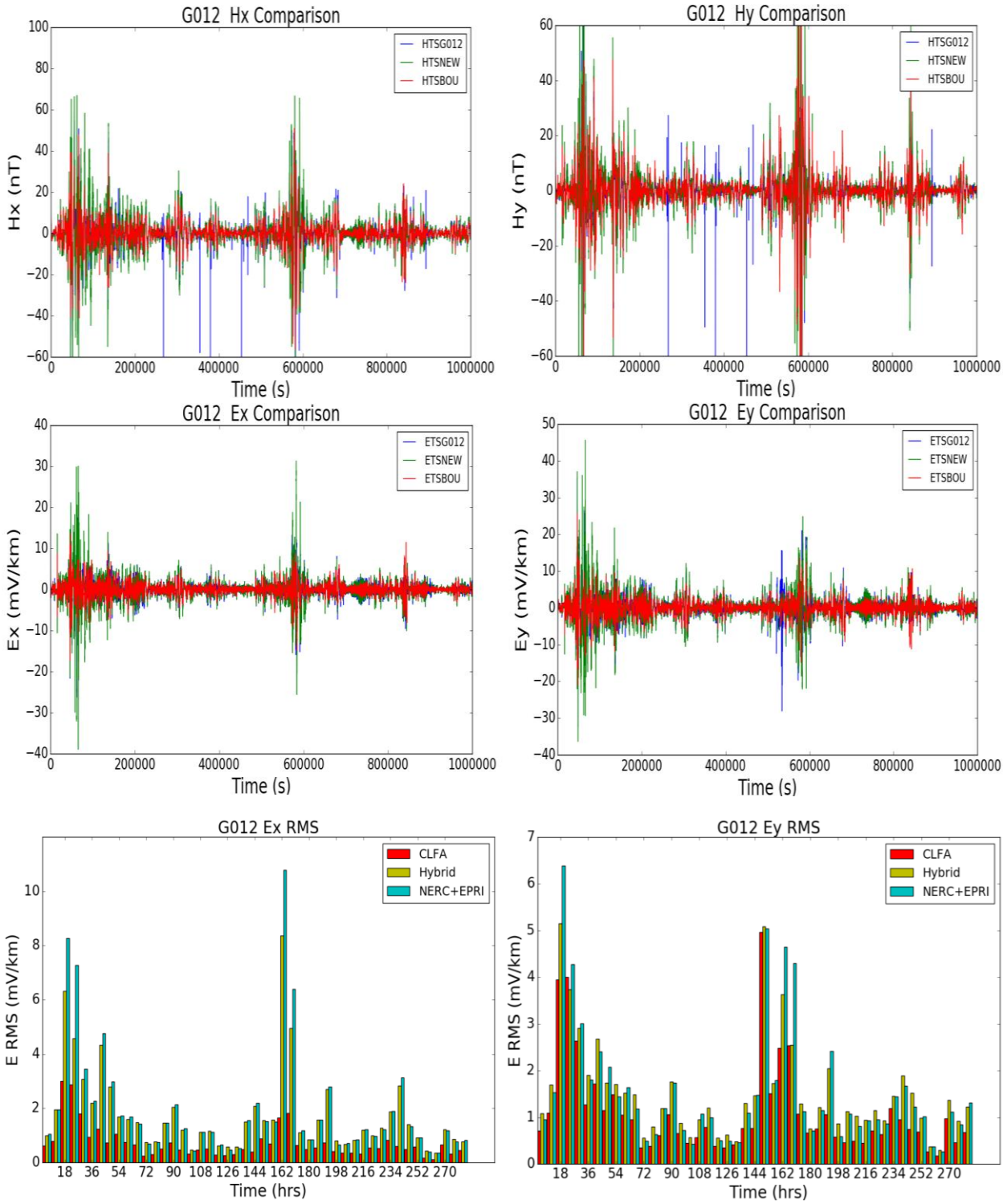

Figure 3.3: Graphs of concurrent magnetic field measurements for the tested signals (top), electric field predictions resulting from magnetic observatory data compared to site G012 measurements (middle), and 6-hour binned RMS misfits between the predicted and measured electric fields for MOCHA site G012 using multiple prediction techniques. Panels on the left side represent fields that are oriented North-South (x), while panels on the right side represent East-West (y).

3.2.2 Regional Scale Amplification and Electric Field Vectors

The general electric field amplification or attenuation for the tested array can be represented by the contour map shown in Fig. 3.4. Electric field predictions for each of the sites were calculated using the CLFA method for two reported GIC event periods. The two periods were April 12 – 14, 2016 and May 7 – 8, 2016. Site electric fields were then converted to an RMS amplitude over each time period, using the equation:

$$RMS = \sqrt{\frac{1}{n}\sum_{i=1}^{n}(Epred_i - Emean)^2} \tag{3.5}$$

where $Epred_i$ is the predicted electric field for time i, and $Emean$ is the average of the n second long predicted electric field time series that represents the GIC event period. RMS amplitude was used to determine the general amplification of the electric field at each site, and these amplifications closely matched the relative magnitudes of the site impedances. Large amplifications occurred at sites with large impedance magnitudes, and vice versa, so these maps serve as a general indicator of locations that are prone to greater electric fields and thus enhanced GIC effects. Each of the site RMS amplitudes were then interpolated using the Nearest Neighbor technique in ArcGIS to produce the contours shown in Fig. 3.4. The North oriented electric fields (*Ex*) were classified into color-coded categories using natural breaks, and then the east oriented fields (*Ey*) were set to the same class ranges to allow for easy comparison between the maps. Based on Fig. 3.4, it is clear that the region is highly 3-D, with several orders of magnitude variation in the electric field amplification for both orthogonal field components. The figure also bears no resemblance to the 1-D conductivity maps that are used in the NERC method, which suggests that electric field predictions will vary greatly with the CLFA method. *Ex* and *Ey* also appear to differ greatly in both magnitude and shape of the amplification. Contours for April and May appear to be very similar, despite May having much larger values due to being a stronger GIC event, which supports the claim that the maps provide a general overview of GIC susceptible areas even with differing input magnetic field values.

With regard to the test cases, the Tillamook-Carlton line is within the higher conductivity resolution region of the finer space (~20 km station spacing vs. ~70 km spacing for the EarthScope Transportable Array) MOCHA data, where greater variations in amplification are observed over small distances. The line is located in a fairly homogeneous area of low

amplification for *Ex*, and a heterogeneous region of greater amplification for *Ey*. The western end of the line has a greater *Ex* and the eastern end has a greater *Ey* amplification, so we would expect a variety of electric fields and GIC effects depending on the values of the input magnetic field. Amplifications in the region spanned by the Pacific DC intertie are very low, except for the southern end of the line, which suggests that the CLFA method will likely produce lower GIC predictions than the NERC method on average. Bus 1 in the WECC circuit test case (Seattle) is close to regions of very high amplification for both *Ex* and *Ey*, and therefore the CLFA method will likely have larger electric field and GIC predictions than the NERC values throughout the tested GIC spike. The rest of the lines and buses in the circuit span a wide variety of amplifications in both electric field directions, so the resulting GIC predictions will be a good test of 3-D effects across large transmission systems. Combining these amplifications with vector maps that show how the electric fields are integrated along the test cases will give more insight into the anticipated results for the subsequent GIC predictions.

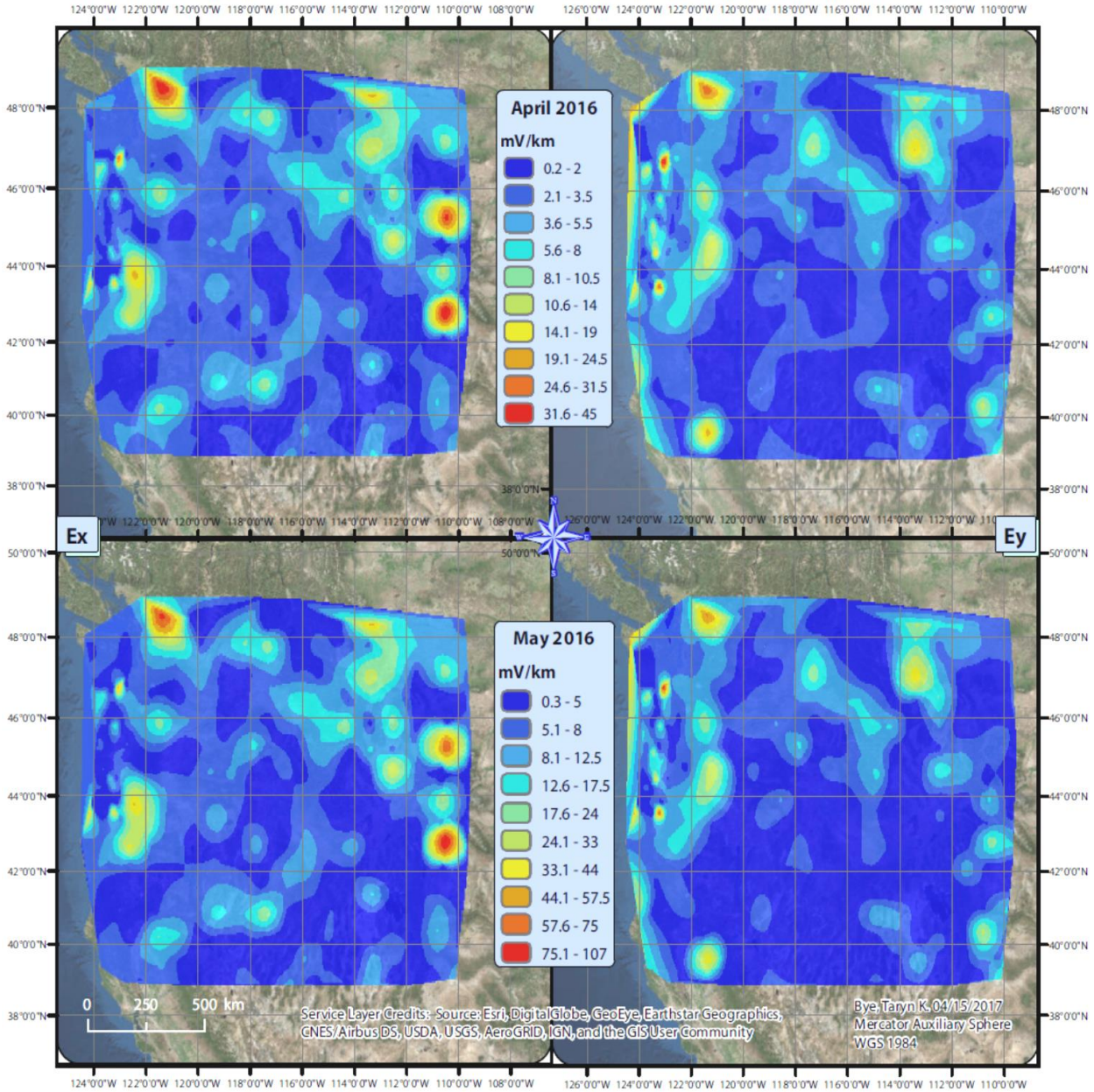

Figure 3.4: Site electric field amplifications for North-South (*Ex*, left) and East-West (*Ey*, right) components over April (top) and May (bottom) GIC events. Amplifications are derived by calculating the RMS amplitude of the site electric field CLFA predictions over the tested time period, and then the amplitudes are interpolated onto adjacent points using the nearest neighbor technique to form contours via ArcGIS. The western portion of the EarthScope Transportable Array and the entire MOCHA MT Array are combined to form the tested data set. These maps were created by Taryn K. Bye for this paper.

The electric field for the entire tested array can also be represented in vector form to show the polarization of the fields with respect to the test case lines. Electric field vectors can be

constructed by first calculating the electric field predictions for every site in the array. In this case, the time was chosen to be the peak of the largest spike during the May, 2016 GIC event. This peak time corresponds to 180 seconds in Fig. 3.6 and will be used for analysis in later sections. Vectors can then be constructed based on the magnitude and angle of the electric field that are derived from the values for *Ex* and *Ey* for each of the sites. The base of the vectors are placed at the corresponding site locations and the lengths are normalized to a given unit vector. The vector plot for this peak time is displayed below in Fig. 3.5. The figure also clearly depicts a highly 3-D region for the CLFA based predictions, which is shown by large variations in vector length i.e. electric field magnitude and vector orientation. Electric field magnitudes generated using the NERC method are all equal within a given 1-D physiographic province, since the impedance is, by definition, invariant within the region. This is illustrated by displaying only 5 different vectors, each representing one of the 5 1-D physiographic regions in this array (as defined using the NERC 1-D guidelines). The NERC guideline-defined electric field vectors also all point in the same direction, whereas the CLFA vectors are not constrained to point in any specific direction, in contrast to the 1-D case where the electric field is always orthoganal to the input magnetic field (NEW). Vector orientation plays a large role in determining the GIC effects that result from the related electric fields, so the map indicates GIC vulnerability in a similar way to the amplification map for a specific time. If the electric field is aligned with a transmission line then the GIC related voltage will be at a maximum, from simply multiplying the magnitude of the field by the line length. If the electric field is perpendicular to the transmission line then it will have no GIC related effects regardless of the magnitude, which demonstrates the importance of electric field orientation in relation to transmission lines. The fact that all NERC produced electric field predictions have the same orientation for a given time seems to be a profound limitation, given that the GIC predictions can be greatly over or under estimated based on the orientation of the transmission line.

The Tillamook-Carlton line is a good example of the effect of electric field and transmission line orientation, in that the CLFA prediction for the eastern end of the line is larger than the NERC prediction, yet it is also nearly perpendicular to the line. Therefore, the CLFA GIC prediction would be expected to be lower despite having a higher overall electric field. The Pacific DC intertie is predominantly oriented in both the NERC and average CLFA field directions, so the deciding factor in GIC prediction differences will be the site field amplitudes.

The WECC circuit has a variety of orientations that seem to cancel out in certain regions for the CLFA vectors, so it will be interesting to see how these cancellations translate into GIC predictions when compared with the non-cancelable NERC results.

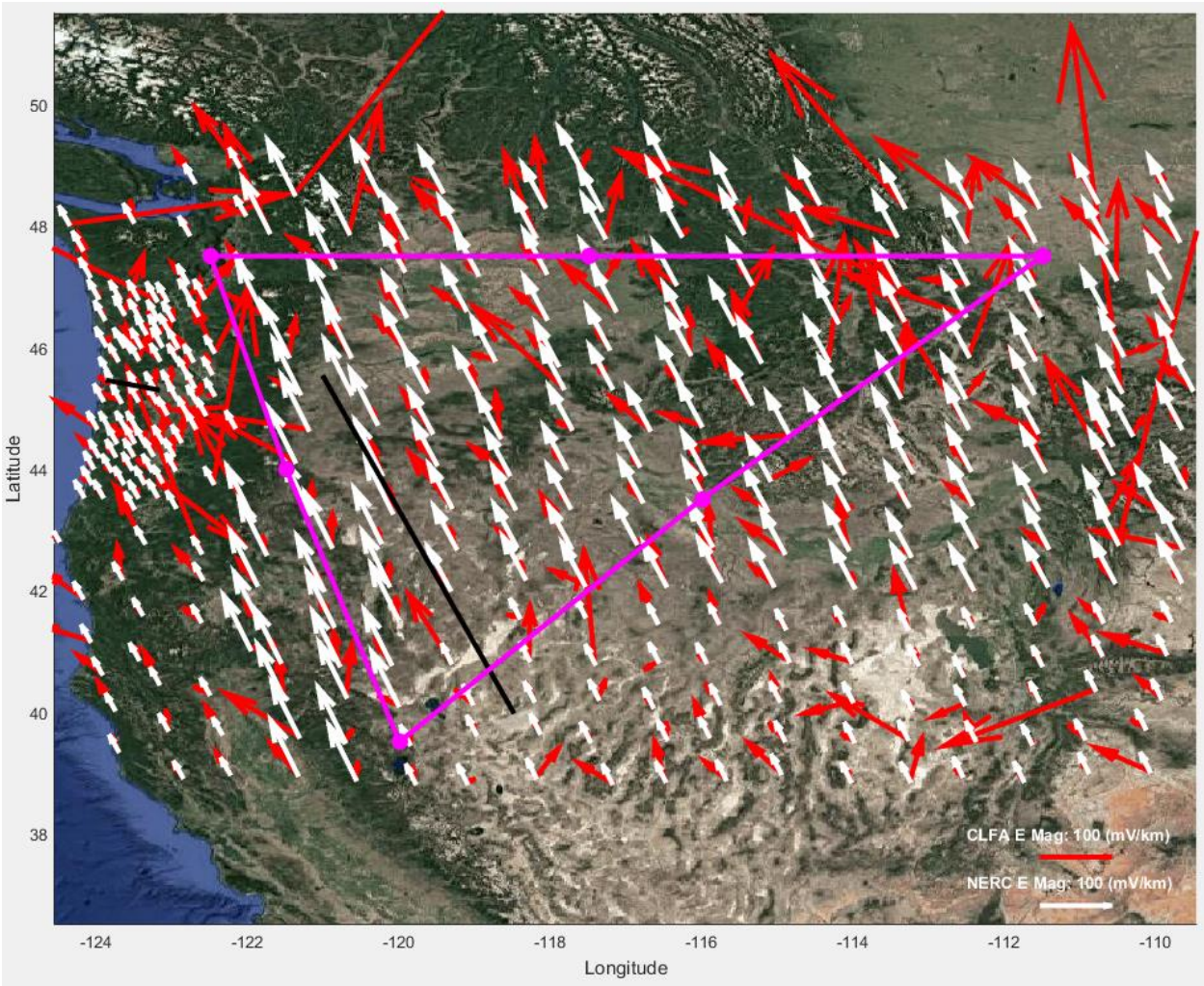

Figure 3.5: Map of EarthScope Transportable Array and MOCHA Project magnetotelluric site locations, with vectors representing the predicted electric fields for those sites at the maximum point of a peak GIC event. CLFA generated vectors are shown in red and NERC generated vectors are shown in white, with both having a unit length of 100 mV/km based on the scale in the bottom right-hand corner of the map. The two line test cases are shown in black, where the Tillamook-Carlton line is further west than the Pacific DC intertie line. Lines and dots represent the WECC circuit test case, and the alignment of the electric field vectors with each test case indicates the relative GIC effect that occurs for the event

3.2.3 Comparison of CLFA and NERC Electric Field Predictions

The last data products to analyze before examining the test cases are the magnetic and electric fields involved in the tested GIC spike. The Newport magnetic observatory data for the spike, and the CLFA and NERC electric field predictions that were produced from that data, are shown in Fig. 3.6. Demonstration sites were selected randomly to represent each of the 5 NERC physiographic province/1-D conductivity regions, with site 1 (dark blue) corresponding to region PB1, 68 (green) to CO1, 126 (red) to BR1, 227 (light blue) to PB2, and 254 (purple) to CS1. These 5 electric field plots represent every NERC prediction for the entire array over the tested 1350 second period. 180 s had the largest overall combined magnitude for *Ex* and *Ey* within the time span, so it was selected as a GIC prediction testing point. GIC spike times of 0, 600, and 1020 seconds from the start of the event were also selected as testing points to cover a range of *Ex* and *Ey* combinations. For *Ex*, site 254 (purple) has almost double the amplitude for the NERC version, while 227 (light blue) has almost double the amplitude for the CLFA version. Other sites, such as 126 (red) are almost identical for the two methods, so the level of amplification or attenuation can vary wildly for the two methods depending on the site. Certain time series structures or shapes are directly attributable to 3-D effects, so greater differences than simple scaling between the site predictions can occur as well. Figs. 3.4 and 3.5 displayed even more extreme examples of differences between the two prediction methods, though knowing the general shape of the time series involved and how they vary visually is still helpful for later interpretation of the test cases.

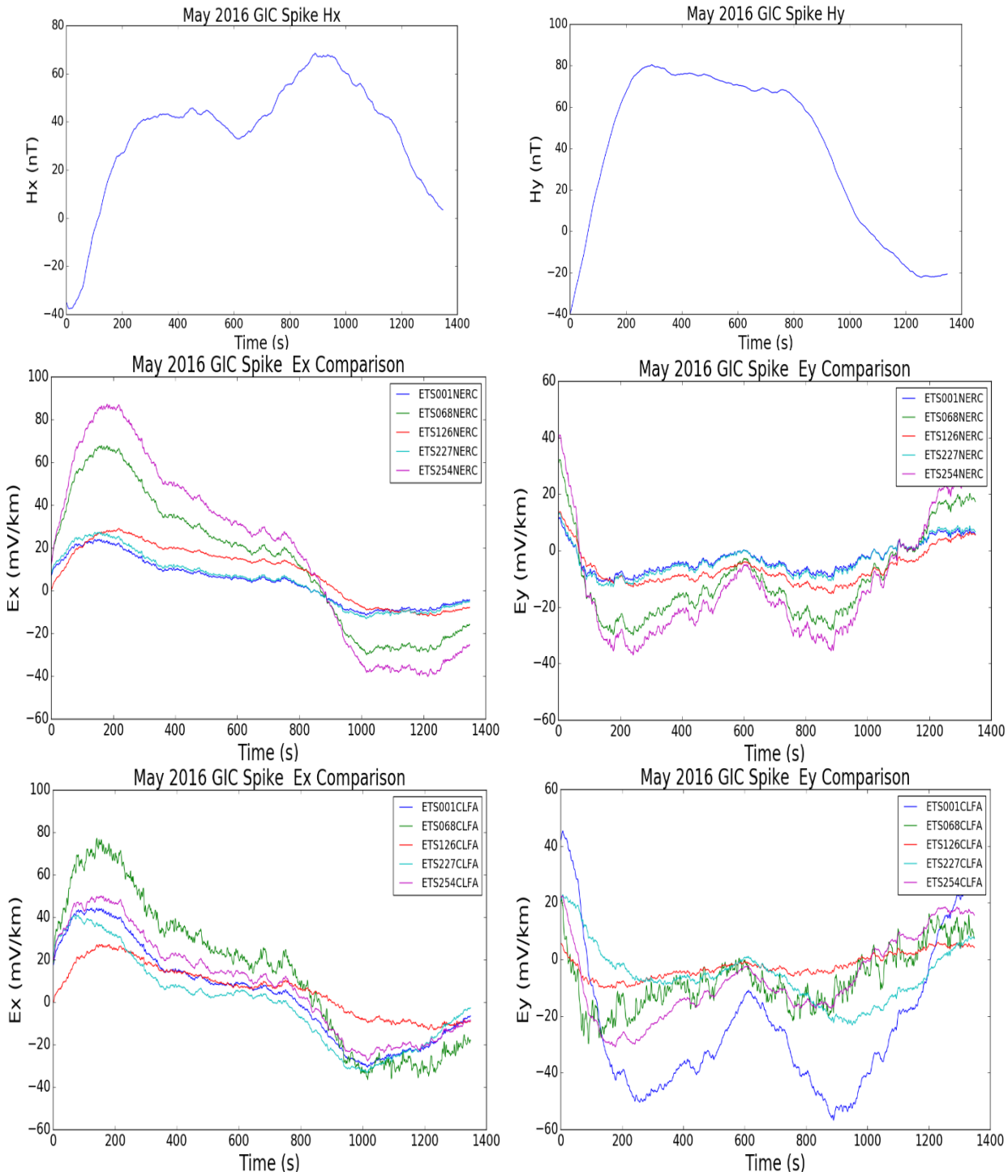

Figure 3.6: Measured North-South (*Hx*) and East-West (*Hy*) magnetic fields for the USGS Newport observatory over the 1350 second tested GIC spike (top), and the resulting *Ex* and *Ey* predictions from inputting those magnetic field measurements into the NERC (middle) and CLFA (bottom) methods. Multiple site electric field predictions are plotted vs. time to show the range of possible NERC predictions across the array and to compare with the corresponding CLFA predictions.

3.2.4 GIC Prediction Test Cases

The final step in the comparison between the CLFA and NERC methods is to show the GIC predictions that result from both techniques, compare the predictions to previous estimates based on the amplification and electric field vectors related to the test cases, and assess any differences that arise from the comparison. GIC predictions are obtained by producing electric field predictions for both methods over the 1350 second peak period. Site predictions are then interpolated onto points representing an evenly spaced grid that spans the latitude and longitude range of the test case system, by using the Delaunay triangulation shown in Fig. 3.2 using a nearest neighbor interpolation scheme. For the Tillamook-Carlton line, this spacing is 0.05 degrees, while the other two cases use 0.5 degree spacing due to larger spacing of surrounding sites and longer line length. Once the electric field predictions are calculated for each of the array points, they are then read into the GIC module for PowerWorld™ and used to predict GIC effects based on the parameters provided in section 3.1.2. GIC losses and current, which is represented for each phase within the 3-phase system, are shown in Figs. 3.7, 3.8, and 3.9 for the three test cases.

The Tillamook-Carlton line is the first to be examined, with the GIC predictions for the CLFA (top) and NERC (bottom) methods depicted in Fig. 3.7. GIC predictions are shown for the peak time of 180 seconds to allow for comparison with the electric field vector map, though the estimate for the CLFA prediction to have lower GIC effects than the NERC method based on vector orientation cannot be easily tested due to CLFA having lower electric field magnitudes for that time. That being said, the 0 second CLFA case has an E magnitude of 0.030 V/km for the eastern substation and 0.004 V/km for the western substation, while the NERC version has 0.014 V/km for both. The total electric field magnitude for the CLFA case is larger, though the NERC version has a total GIC loss prediction of 0.040 MVAR vs. 0.025 MVAR for the CLFA method. The vector plot for 0 seconds also shows the CLFA based eastern electric field vector being nearly perpendicular to the test case line, which supports the original claim that vector orientation is a large factor for GIC strength, in that it can cause higher electric fields to have lower GIC effects or vice versa. Regarding electric field amplification, the CLFA western end has a larger electric field when Ex is greater and a larger eastern field for greater Ey, which follows the estimates of amplification being stronger for Ex in the west and Ey in the east. The

NERC tests each have the same electric field magnitude across the line, due to each of the interpolation points being located within the same 1-D conductivity NERC-defined physiographic province. This identical electric field causes the GIC current, voltage, and losses to simply scale with the electric field magnitude. Comparing the two GIC prediction methods in Fig. 3.7 shows that the NERC approach can produce roughly 3 times greater GIC current, voltage, and losses than the CLFA technique with the same input magnetic field. The CLFA method can also produce far larger GIC predictions than the NERC technique, as is shown by the GIC losses being 0.034 MVAR vs. 0.006 MVAR for the two methods respectively during the 600 second case.

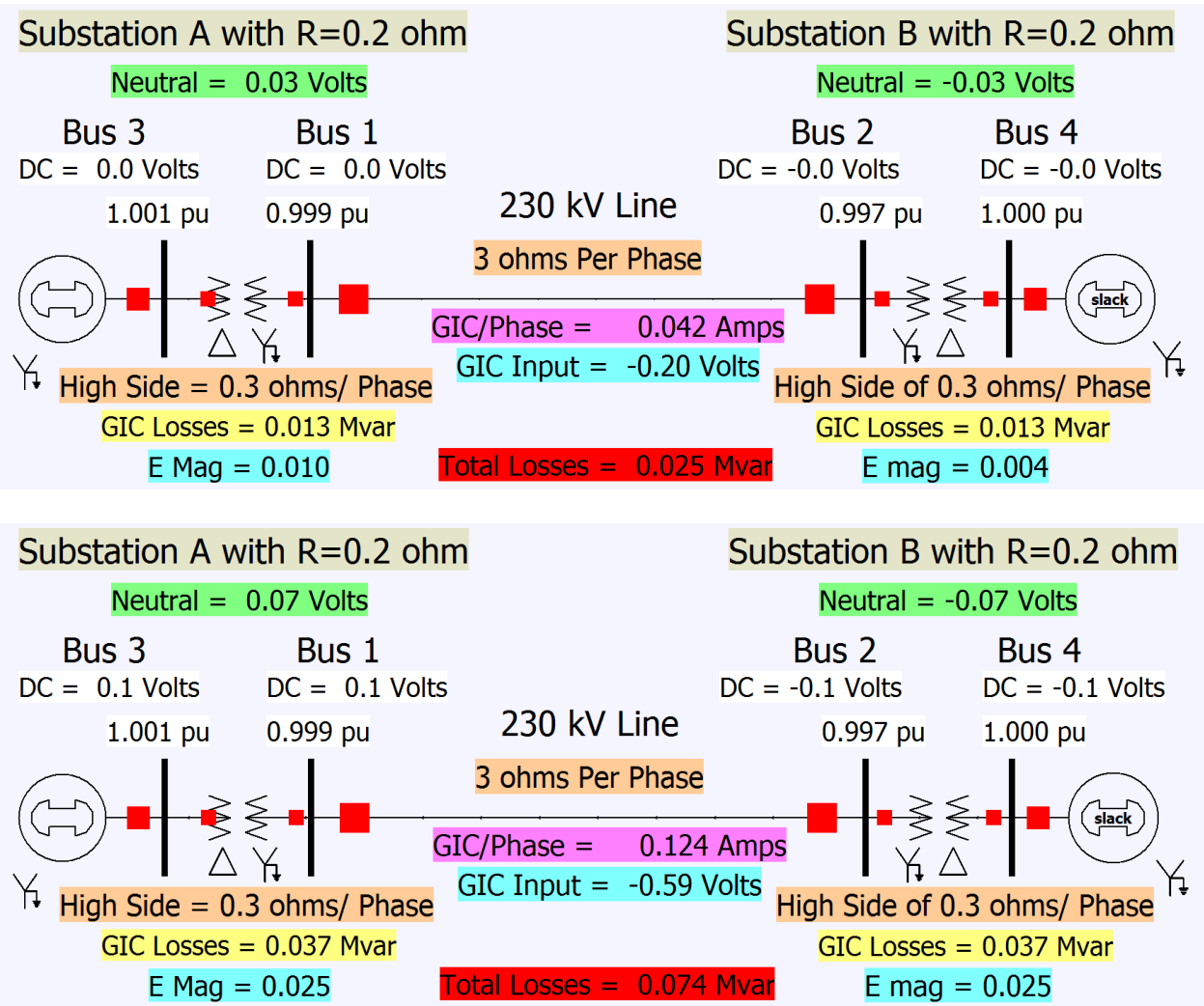

Figure 3.7: GIC predictions based on CLFA (top) and NERC (bottom) electric field predictions for the peak of the May, 2016 GIC event (180 s) for the Tillamook-Carlton test case. Predictions were generated using PowerWorld^{TM} with standard GIC parameters used in the example case that is included with the software.

The Pacific DC Intertie is examined next, with the GIC predictions for the CLFA (top) and NERC (bottom) methods portrayed in Fig. 3.8. Based on the amplification map, it was estimated that the CLFA electric field magnitudes would be similar or less than the NERC values, due to the test case line being in a region of 3-D attenuation. From Fig. 3.8, and the fact that every other tested time followed this trend, the amplification prediction seems to be correct. Both methods generated larger GIC predictions than the Tillamook-Carlton line values, despite the Pacific DC intertie having lower electric fields and amplification, though the larger values can be attributed to the intertie being longer and thus integrating more electric field values over its distance. The closer alignment of the NERC vectors with the test case line also suggested that the NERC GIC predictions would be larger than the CLFA ones for similar electric field magnitudes, which is also seen in Fig. 3.8, in addition to the other tested times. Comparing the two methods directly yields the observation that the NERC method predicts larger GIC events on average than the CLFA technique for this test case, though the differences in predictions are much smaller than for the Tillamook-Carlton line.

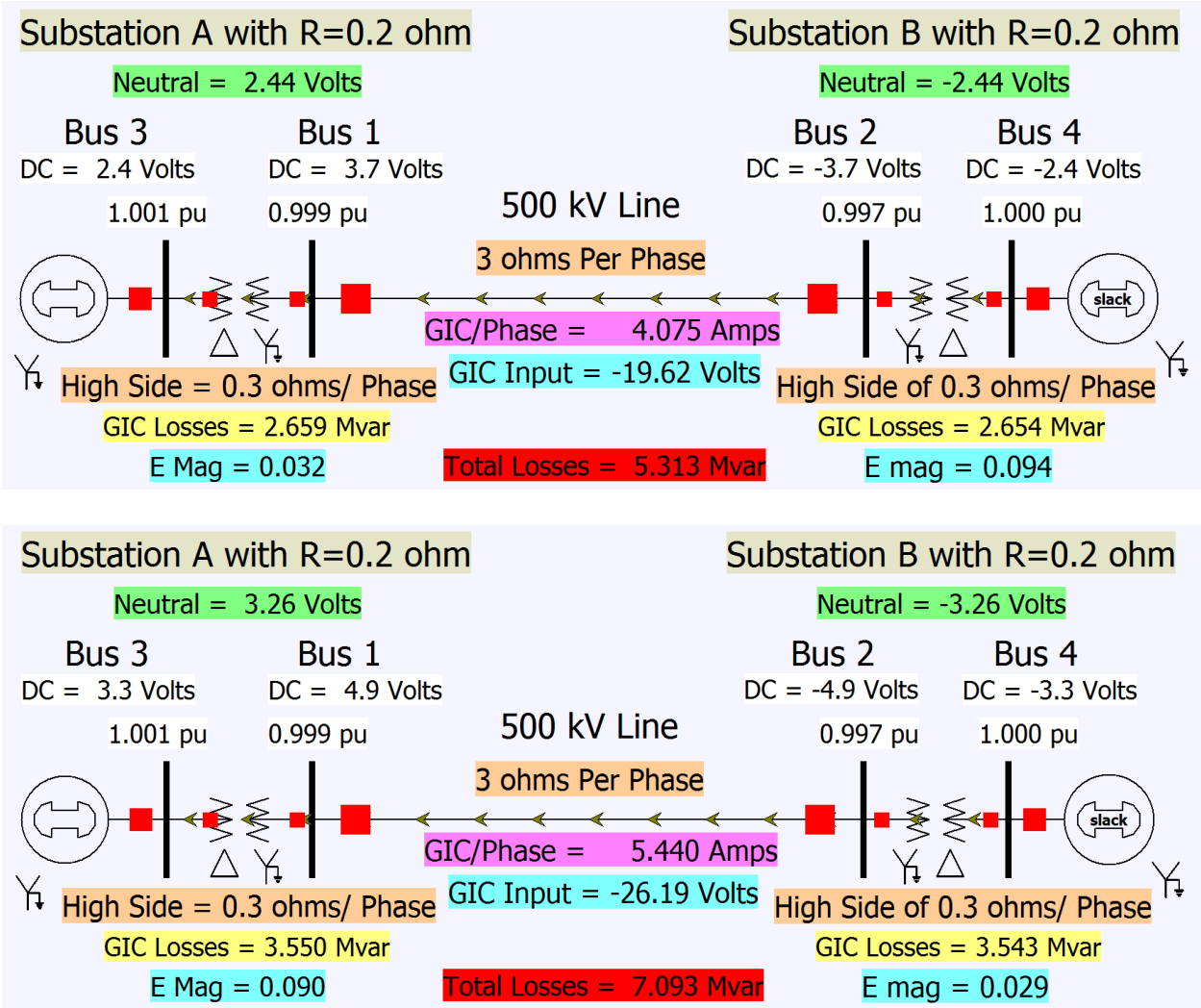

Figure 3.8: GIC predictions based on CLFA (top) and NERC (bottom) electric field predictions for the peak of the May, 2016 GIC event (180 s) for the Pacific DC Intertie test case. Predictions were generated using PowerWorld^{TM} with standard GIC parameters used in the example case that is included with the software.

The WECC test circuit is the final case that is examined, with the GIC predictions for the CLFA (top) and NERC (bottom) methods depicted in Fig. 3.9. It was difficult to provide any predicted outcomes of GIC effects for the two methods based on the amplification and vector maps, given that the circuit spanned a large variety of electric field values and orientations, though it was estimated that Seattle (Buses 2 & 7) would have a large CLFA electric field and that the CLFA vectors could potentially cancel out over portions of the line to yield seemingly 1-Dimensional effects. Fig. 3.9 shows Seattle having a more than 3 times greater electric field magnitude for the CLFA prediction than the NERC value, which supports the amplification map

once again. The GIC/Phase currents are very similar for both methods, aside from the transmission lines running from Bus 7 to Bus 4, which is near the Pacific DC intertie and shares many properties with it like the NERC method having larger predictions. GIC effect predictions are lower for the circuit than the Pacific DC intertie, despite having larger electric field magnitudes and line lengths, due to the circuit using a lower nominal voltage (230 vs. 500 kV) and different line resistances. Both test cases have roughly the same percentage difference of 50% between the CLFA and NERC methods, which is surprising considering that the circuit covers a larger range of more heterogeneous material that enables varied electric fields between the two techniques. The similarity in GIC currents and total losses for the circuit relative to the other test cases seems to suggest that 3-D conductive effects may actually cancel out over long distances or large systems, or at least the differences in GIC predictions seem to decrease based on this trend. Individual losses and GIC effects for specific line arrangements or situations can still generate large differences in predictions between the two methods, though this will be discussed in the next section.

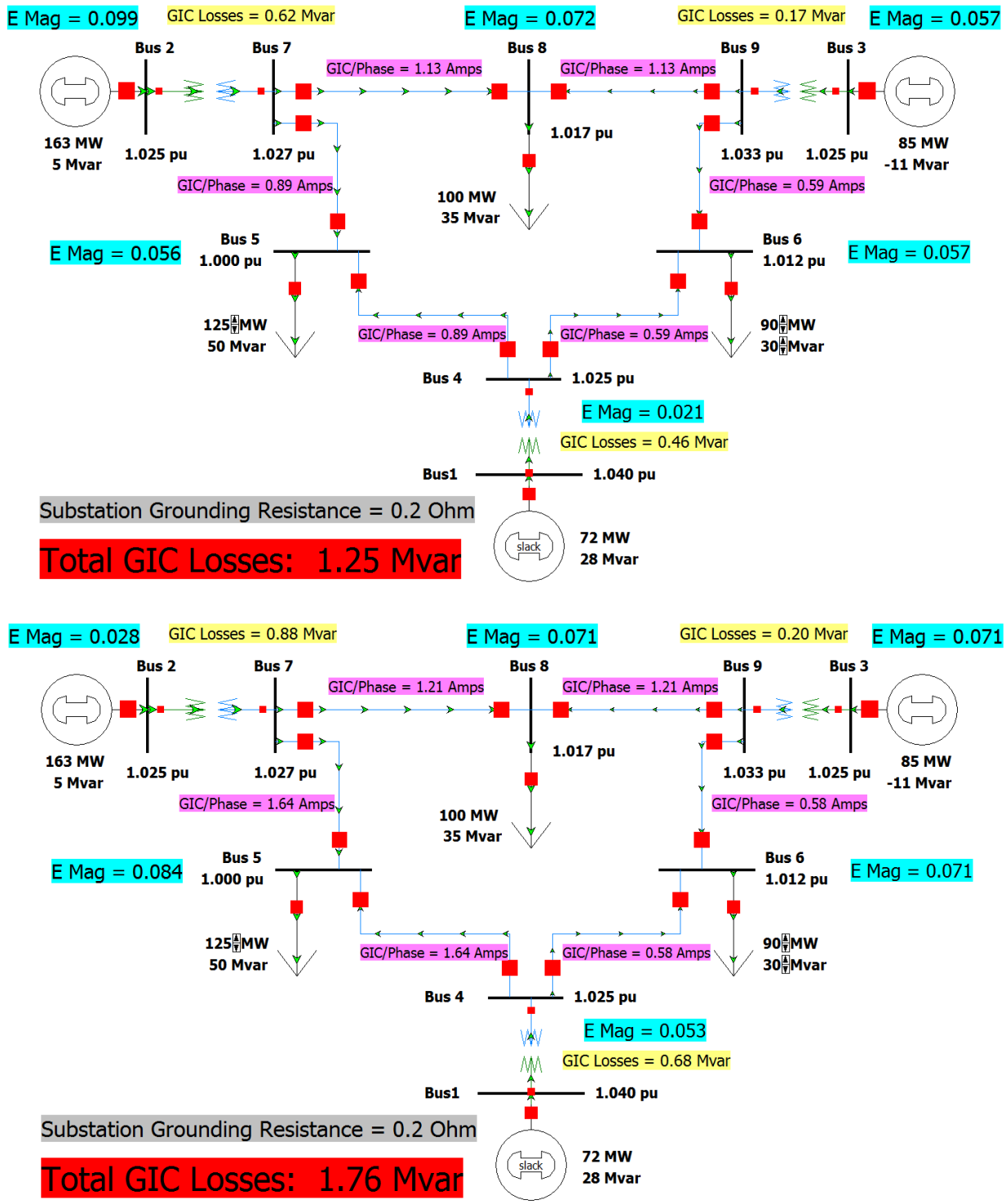

Figure 3.9: GIC predictions based on CLFA (top) and NERC (bottom) electric field predictions for the peak of the May, 2016 GIC event (180 s) for the WECC circuit test case. Predictions were generated using PowerWorld with standard transformer GIC parameters and line resistances matching the original test case.

3.3. Discussion

The primary limitations involved in the Cascading Linear Filter Algorithm (CLFA) method, and the related applications discussed in this paper, are the reliance on USGS Geomagnetism Program server data for analysis, the need for high-pass filtering of time series data, and the use of stock test case values for GIC prediction. Based on our experience, it takes an average of 10 to 15 seconds to receive data from the USGS Geomagnetism server, regardless of the requested data length or internet speed, which can hinder real-time predictive capabilities. 1-second USGS magnetic observatory data also needs to exist for the time period that a site was originally occupied for the full CLFA method to be possible, though reasonable predictions are still possible without as is shown in the results section. If the USGS server latency proves prohibitive, then a local site in the tested area could be operated to provide real-time data via telemetry. If a previous EarthScope magnetotelluirc (MT) array station was chosen for continual operation then the full CLFA method would be possible even for sites run before the advent of 1-second USGS data, through comparing the original site time series with other concurrent sites to establish transfer functions. Using a previously occupied site would also provide local electric field noise to combine with predictions to increase accuracy. The NERC method also relies on USGS magnetic observatory data and therefore has these same real-time limitations, with both methods having similar computational speeds and loads as well. Both methods were found to produce 100,000 second electric field predictions within a second of run time for a single site on an outdated desktop computer, though the NERC method would perform quicker for a set of closely spaced interpolation points where each could be simply represented with the regional values. The CLFA method could still run in real-time for this case on a server or with better parallelization, so it is fair to conclude that both methods can be implemented for real-time GIC predictions. CLFA based predictions also require high-pass filtering with a corner frequency of 10^{-4} Hz to remove diurnal drift and spectral leakage, so predictions are not based on the full measured data. GIC spikes are often stronger than diurnal variations, which means that filtered electric fields can still be fairly accurate for GIC predictions, though long-period improvements can be made such as extending the impedance through global 3-D mantle conductivity models [Kelbert *et al.*, 2009; Sun *et al.*, 2015]. Attempts were made to extend the magnetic transfer function frequency bands by using very large windows, i.e. 200,000 seconds, and/or down-sampling or low-pass filtering the entire recorded site time series for use in processing. Spectral

leakage and large offsets between windows were still observed despite these efforts, because the short duration of site occupation was found to limit the statistical strength of band-averaging for the lowest frequencies. As for the GIC predictions, the use of stock GIC parameters provided with the simulation code and the wide range of possible values had a large effect on the resulting output. This effect essentially caused the predictions to be meaningless, aside from the ability to compare between different methods by using the same parameters. If a standard GIC test were to be developed, or if the CLFA method were applied to a real power system, then accuracy of the proposed technique could be tested, rather than basing conclusions off of a comparison with the industry standard NERC model.

Comparisons between the GIC predictions for the CLFA and NERC methods showed a variety of discrepancies for multiple test cases located within the EarthScope and MOCHA magnetotelluric arrays. It was previously shown [Bonner & Schultz, 2017] that the CLFA method produces electric field predictions with far greater fit to tested sites within the MOCHA array than the NERC technique for locations with heterogeneous conductive structure, and equal fit for areas of relative homogeneity. Given that the CLFA method produces equal or better predictions than the NERC method, it seems reasonable to conclude that differences in electric field predictions between the two methods are the result of limitations in the NERC procedure of using regional 1-D models in highly 3-D areas with large local variation. Based on this conclusion, discrepancies in the GIC predictions that are derived from these electric field predictions would also be the result of that limitation. For the Tillamook-Carlton line test case, GIC effects were found to be up to 3 times larger for one method compared to the other over the span of a 1350 second GIC spike. If the GIC event had a 1 V/km electric field strength like in typical testing, or especially a 100-year storm that would be able to produce a 5 - 20 V/km field depending on the ground conductivity structure [Pulkinnen *et al.*, 2012; Love *et al.*, 2016], instead of the moderate event tested here then the discrepancy in predictions could have caused massive damage if the NERC method was used. In fact, the Tillamook-Carlton line has had problems in the past from incorrect GIC predictions [Kappenman & Radasky, 2014], which motivated its selection as a test case for the present paper. It is difficult to determine whether greater conductivity resolution from closer site spacing, shorter line length, or larger variation in ground conductivity was the cause of the case having larger discrepancies than the other tests, though it is clear that there are certainly situations where 3-D effects do not average out. Electric

field vector orientation in relation to the tested transmission line was also shown to be important for determining GIC effects. NERC based electric field predictions are always oriented perpendicular to the input magnetic field, which makes the GIC predictions largely dependent on the orientation of the test case line, while CLFA predictions work for any orientation. This limitation was addressed with the claim that 3-D effects averaged out over long transmission distances, yet our Pacific DC intertie test case clearly showed an up to 50% systematic overprediction of NERC based GIC effects due to the 1-D vectors consistently matching the line orientation better than the 3-D vectors. The WECC circuit case also showed up to a 50% mismatch between the two prediction methods, though the test case included far more transmission length, so the claim of averaging 3-D effects may have some validity for very long systems or certain system geometries. Even with this possibility, large local deviations between the two methods are possible under certain circumstances that can cause the NERC technique to be dangerously inaccurate.

3.4. Conclusion

Comparisons of both electric field and GIC predictions for the proposed Cascading Linear Filter Algorithm (CLFA) and the industry standard NERC methods were examined to assess limitations and potential implications of both techniques. The CLFA method projects observatory magnetic field variation measurements through a multi-station observatory-to-site transfer function to yield local magnetic field predictions for a set of previously operated MT stations. The magnetic field predictions are then projected through the corresponding 3-D site impedance tensors to produce site electric field predictions that are interpolated onto a tested power system within the MT site array. Predicted electric fields at points representing the power system can then be input into a power flow simulator to produce GIC predictions. Although the NERC method involves a similar work flow, it instead projects the closest magnetic observatory data through a 1-D regional impedance. As previously demonstrated, the NERC method produces far less accurate results than the CLFA technique in conductively heterogeneous areas [Bonner & Schultz, 2017], so the next step was to determine how electric field prediction accuracy corresponded to GIC effects for various test cases. Findings indicate that GIC predictions for one method could be up to 3 times larger than for the other method in the Tillamook-Carlton line, and 1.5 times larger for the Pacific DC intertie and WECC circuit test

cases. 3-D electric field amplification and non-perpendicular vector orientation were found to be primary explanatory factors for discrepancies between the two methods, with maps of these values serving as useful diagnostic tools for assessing GIC risk of locations within the tested array. Discrepancies were tied to limitations with the 1-D NERC method being applied to highly 3-D conductivity regions, such as the Northwestern United States, and consequences of such discrepancies during strong GIC events were considered. It is clear that 3-D electric effects do not reliably average out over long transmission lines in a manner enabling the NERC method to effectively protect grids located within conductively heterogeneous areas. Given that both methods have generally comparable computational speed and burden, the proposed CLFA method would improve grid reliability for areas covered by the EarthScope Transportable Array if implemented.

4 General Conclusion

In this study, a computationally quick and light geomagnetically induced current (GIC) prediction algorithm is proposed, analyzed for validity, and compared against the NERC industry standard method for multiple situations. Chapter 1 established the basic concepts and framework for the thesis, while Chapters 2 and 3 explored features of the algorithm. Chapter 2 demonstrated the results and error involved with each step of the algorithm to test and address any limitations with the technique. Magnetic and electric field predictions generated from the proposed Cascading Linear Filter Algorithm (CLFA) were compared against concurrent site measurements to estimate prediction accuracy. Electric field predictions for the CLFA method were also compared with regional 1-Dimensional conductivity based NERC + EPRI (NERC) predictions to assess the validity of both techniques. The CLFA method was found to have greatly lower RMS misfit than the NERC method when compared to measurements for the tested sites, in addition to both methods having comparable computational speeds. This accuracy discrepancy was attributed to the highly 3-D conductivity structure of the tested region, which could not be adequately represented by the regional 1-D model that was implemented in the NERC method.

In Chapter 3, the electric field predictions for the CLFA and NERC methods were used to generate GIC predictions for test cases located in the same tested region. Electric field predictions for both methods were also used to construct site amplification and field vector maps, which showed effective GIC susceptibility of locations within the tested array. GIC predictions for three test cases; including representations of the Tillamook-Carlton line, a portion of the Pacific DC intertie, and a simplification of the WECC system, were produced and found to generally agree with the preceding maps. The Tillamook-Carlton line, which was the shortest line and had the highest conductivity resolution, was determined to have up to 3 times higher or lower electric field predictions, GIC currents, and reactive power losses for the CLFA values compared to the NERC ones. The other two test cases were found to have up to 1.5 times greater or lower discrepancies in GIC predictions as well, which rejects the hypothesis that GIC effects average out over long or large power systems. Moreover, local discrepancies between the prediction methods were large even when the overall GIC effects were similar. GIC prediction discrepancies between the two methods were attributed to limitations in the NERC technique,

given that Chapter 2 demonstrated that the CLFA method produced far more accurate electric field predictions in this region, which suggests that current industry predictions could have large enough errors to prevent effective GIC mitigation. Use of the NERC method in conductively heterogeneous areas such as the Pacific Northwest therefore poses a concern for the reliability of the power grid, though additional work involving GIC prediction comparisons for real power grids is needed to firmly establish this risk and assess the utility of the CLFA method.

REFERENCES

AL-Hinai, A. (2000), Voltage Collapse Prediction for Interconnected Power Systems, Master of Science Thesis, Department of Electrical Engineering, West Virginia University, West Virginia, USA.

Bahr, K. (1988), Interpretation of the magnetotelluric impedance tensor: Regional induction and local telluric distortion, J. Geophs., 62, 119–127.

Barber, C., et al. (1996), The Quickhull algorithm for convex hulls, Acm. T. Math. Software, 22, 469–483.

Bedrosian, P. A., and J. J. Love (2015), Mapping geoelectric fields during magnetic storms: Synthetic analysis of empirical United States impedances, Geophys. Res. Lett., 42, 10,160–10,170, doi:10.1002/2015GL066636.

Birchfield, A., et al. (2017), Statistical considerations in the Creation of Realistic Synthetic Power Grids for Geomagnetic Disturbance Studies, IEEE Trans. Power Systems, 32 1502 – 1510.

Bonneville Power Administration (2000), The Pacific Intertie Scheme, [Available at https://web.archive.org/web/20050426045806/http://www.transmission.bpa.gov/cigresc14/Compendium/PACIFIC.htm accessed on April 23, 2017].

Bonner, L R., IV, and A. Schultz (2017), Rapid prediction of electric fields associated with geomagnetically induced currents in the presence of three-dimensional ground structure: Projection of remote magnetic observatory data through magnetotelluric impedance tensors, Space Weather, 15, doi:10.1002/2016SW001535.

Boteler, D. (2014), Methodology for simulation of geomagnetically induced currents in power Systems, J. Space Weather Space Clim., 4, A21.

Boteler, D., R. Pirjola, and H. Nevalinna (1998), The effects of geomagnetic disturbances on electrical systems at the Earth's surface, Adv. Space Res., 22, 17–27.

Burstinghaus, E. (2013), The Importance of Non-Uniform Geoelectric Fields in Calculating GIC Distributions, IEEE Power and Energy Society General Meeting.

Cagniard, L. (1953), Basic theory of the magneto-telluric method of geophysical prospecting, Geophysics, 18, 603–635.

Chave, A., and D. Thomson (2004), Bounded influence magnetotelluric response function estimation, Geophys. J. Int., 157, 988–1006.

Cherevatova, M., M. Y. Smirnov, T. Korja, L. B. Pedersen, J. Ebbing, S. Gradmann, and M. Becken, and MaSca Working Group (2015), Electrical conductivity structure of north-

west Fennoscandia from three-dimensional inversion of magnetotelluric data, Tectonophysics, 653, 20–32, doi:10.1016/j.tecto.2015.01.008.

de Villiers, J., and P. Cilliers (2014), Applying inversion techniques to derive source currents and geoelectric fields for geomagnetically induced current calculations, Ann. Geophys., 32, 1263–1275.

Egbert, G., and J. Booker (1986), Robust estimation of geomagnetic transfer functions, Geophys. J. Roy. Astron. Soc., 87, 173–194.

Eisel, M., and G. D. Egbert (2001), On the stability of magnetotelluric transfer function estimates and the reliability of their variances, Geophys. J. Intl., 144, 65–82.

Electric Power Research Institute (EPRI) (2002), One-Dimensional Earth Resistivity Models for Selected Areas of Continental United States and Alaska, edited by R. Lordan, 1026430, EPRI, Palo Alto, Calif.

Evans, R., et al. (2014), Electrical structure of the central Cascadia subduction zone: The EMSLAB Lincoln line revisited, Earth Planet. Sci. Lett., 402, 265–274.

Gamble, T., W. Goubau, and J. Clarke (1979), Magnetotellurics with a remote magnetic reference, Geophysics, 44, 53–68.

Geomag Library (2016), An Open Source Python Library provided by the US Geological Survey Geomagnetism Program. [Available at https://github.com/usgs/geomag-algorithms accessed on September 1.]

Glover J., M. Sarma, and T. Overbye (2012), Power System Analysis and Design, Fifth Edition.

Groom, R. W., and R. C. Bailey (1989), Decomposition of magnetotelluric impedance tensors in the presence of local three-dimensional galvanic distortion, J. Geophys. Res., 94(B2), 1913–1925, doi:10.1029/JB094iB02p01913.

Horton, R., et al., (2012), A Test Case for the Calculation of Geomagnetically Induced Currents, IEEE Trans. Power Delivery, 27, 2368–2373.

ICSEG (2017), Synthetic Power Grid Test Cases. [Available at icseg.iti.illinois.edu/power-cases/ Accessed on April 23, 2017].

Imamura, N., and A. Schultz (2015), Full waveform time domain solutions for source and induced magnetotelluric and controlled-source electromagnetic fields using quasi equivalent time domain decomposition and GPU parallelization, Abstract GP24A-01 presented at 2015 Fall Meeting, AGU, San Francisco, Calif., 14-18 Dec.

Janssen, A., et al. (1986), Adaptive interpolation of discrete-time signals that can be modeled as autoregressive processes, IEEE Trans Acoust, 34, 317–330.

Jones, A., et al. (1989), A comparison of techniques for magnetotelluric response function estimation, J. Geophys. Res., 94(14), 201–14,213.

Jones, A. G. (2011), Three-dimensional galvanic distortion of three-dimensional regional conductivity structures: Comment on three-dimensional joint inversion for magnetotelluric resistivity and static shift distributions in complex media by Yutaka Sasaki and Max A. Meju, J. Geophys. Res., 116, B12104, doi:10.1029/2011JB008665.

Jones, A. G., et al. (2008), Southern African lithospheric geometries deduced from electromagnetic imaging: The SAMTEX project, Geophys. Res. Abstracts, 10, EGU2008-A-08560, SRef-ID: 1607-7962/gra/EGU2008-A-08560.

Kappenman, J. and W. Radasky (2014), Examination of NERC GMD Standards and Validation of Ground Models and Geo-Electric Fields Proposed in this NERC GMD Standard.

Kataoka, R., and A. Pulkkinen (2008), Geomagnetically induced currents during intense storms driven by coronal mass ejections and corotating interacting regions, J. Geophys. Res., 113, A03S12, doi:10.1029/2007JA012487.

Kelbert, A., A. Schultz, and G. Egbert (2009), Global electromagnetic induction constraints on transition-zone water content variations, Nature, 460, 1003–1006, doi:10.1038/nature08257.

Kelbert, A., G. D. Egbert, and A. Schultz (2011), IRIS DMC data services products: EMTF, The magnetotelluric transfer functions, doi:10.17611/DP/EMTF.1.

Kelbert, A., G. D. Egbert, and C. deGroot-Hedlin (2012), Crust and upper mantle electrical conductivity beneath the Yellowstone Hotspot Track, Geology, 40.5, 447–450.

Khosravi, L., and E. Johansson (2015), Evaluation of the GIC module in PSS/E, Master of Science Thesis, Department of Energy and Environment, Chalmers University of Technology, Gothenburg, Sweden.

Ku, H. H. (1966), Notes on the use of propagation of error formulas, J Res. Nat. Bur. Stand. – C. Eng. Instrum., 70C(4), 263–273.

Lotz, S., and P. Cilliers (2015), A solar wind-based model of geomagnetic field fluctuations at a mid-latitude station, Adv. Space Res., 55, 220–230.

Love, J., and A. Swidinsky (2014), Time causal operational estimation of electric field induced in the Earth's lithosphere during magnetic storms, Geophys. Res. Lett., 41, 2266–2274, doi:10.1002/2014GL059568.

Love, J. J., et al. (2016), Geoelectric hazard maps for the continental United States, Geophys. Res. Lett., 43, 9415–9424, doi:10.1002/2016GL070469.

Meqbel, N., et al. (2014), Deep electrical resistivity structure of the northwestern U.S. derived from 3-D inversion of USArray magnetotelluric data, Earth Planet. Sci. Lett., 402, 290–304.

Molinski, T. (2002), Why utilities respect geomagnetically induced currents, JASTP, 64, 1765–1778.

North American Electric Reliability Corporation (NERC) (2013), Application Guide Computing Geomagnetically-Induced Current in the Bulk Power System, pp. 1–39.

North American Electric Reliability Corporation (NERC) (2016), Benchmark Geomagnetic Disturbance Event Description, pp. 1–25.

Ngwira, C., et al. (2013), Extended study of extreme geoelectric field event scenarios for geomagnetically induced current applications, Space Weather, 11, 121–131, doi:10.1002/swe.20021.

Ngwira, C., et al. (2015), Characteristics of extreme geoelectric fields and their possible causes: Localized peak enhancements, Geophys. Res. Lett., 42, doi:10.1002/2015GL065061.

Overbye, T.J., et al. (1995), A User-Friendly Simulation Program for Teaching Power System Operations, IEEE Transactions on Power Systems, 10(4), 1725–1733.

Overbye, T. J., T. R. Hutchins, K. Shetye, J. Weber, and S. Dahman (2012), Integration of geomagnetic disturbance modeling into the power flow: A methodology for large-scale system studies, North American Power Symposium (NAPS), doi:10.1109/NAPS.2012.6336365.

Overbye, T., et al. (2013), Power Grid Sensitivity Analysis of Geomagnetically Induced Currents, IEEE Trans. Power Systems, 28, 4821–4828.

Pirjola, R. (2002), Fundamentals about the flow of geomagnetically induced currents in a power system applicable to estimating space weather risks and designing remedies, JASTP, 64, 1967–1972.

Pirjola, R., D. Boteler, et al. (2000a), Prediction of geomagnetically induced currents in power transmission systems, Adv. Space Res., 26, 5–14.

Pirjola, R., A. Viljanen, et al. (2000b), Space weather risk in power systems and pipelines, Phys. Chem. Earth, 25, 333–337.

PowerWorld™ Corporation (2011), PowerWorld™ Simulator Version 16 Users Guide.

Pulkkinen, A., O. Amm, and A. Viljanen (2003), Ionospheric equivalent current distributions determined with the method of spherical elementary current systems, J. Geophys. Res., 108, SIA, doi:10.1029/2001JA005085.

Pulkkinen, A., et al. (2005), Geomagnetic storm of 29–31 October 2003: Geomagnetically induced currents and their relation to problems in the Swedish high-voltage power transmission system, Space Weather, 3, S08C03, doi:10.1029/2004SW000123.

Pulkkinen, A., R. Pirjola, and A. Viljanen (2007a), Determination of ground conductivity and system parameters for optimal modeling of geomagnetically induced current flow in technological systems, Earth Planets Space, 59, 999–1006.

Pulkkinen, A., et al. (2007b), First-principles modeling of geomagnetically induced electromagnetic fields and currents from upstream solar wind to the surface of the Earth, Ann. Geophys., 25, 881–893.

Pulkkinen, A., et al. (2012), Generation of 100-year geomagnetically induced current scenarios, Space Weather, 10, S04003, doi:10.1029/2011SW000750.

Pulkkinen, A., et al. (2015), Regional-scale high-latitude extreme geoelectric fields pertaining to geomagnetically induced currents, Earth Planets Space, 67, 93.

Schultz, A. (2009), EMSCOPE: A continental scale magnetotelluric observatory and data discovery resource, Data Sci. J., 8, P IGY6-IGY20, doi:10.2481/dsj.GG_IGY-009.

Schultz, A., and G. Pritchard (1999), Three-dimensional inversion for large-scale structure in a spherical domain, in Three Dimensional Electromagnetics, SEG Geophysical Developments Series 7, pp. 451–476.

Schultz, A., P. Bedrosian, K. Key, D. Livelybrooks, G. D. Egbert, E. Bowles-Martinez, and P. E. Wannamaker (2014), Magnetotelluric investigations of convergent margins and of incipient rifting: Preliminary results from the EarthScope MT Transportable Array and MT FlexArray deployments in Cascadia and in the North American Mid-Continent Region, Abstract GP31A-3676 presented at 2014 Fall Meeting, AGU.

Siemens Energy, Inc. (2016), PSS®E Xplore 34 Users Guide.

Simpson, J. J. (2009), Current and future applications of 3-D Global Earth-Ionosphere models based on the full-vector Maxwell's equations FDTD method, Surv. Geophys., 30(2), 105–130.

Stearns, S. D., and D. R. Hush (1990), Digital Signal Analysis (Prentice Hall Signal Processing Series), 2nd ed., 460 pp., Prentice Hall, Englewood Cliffs, N. J.

Sun, J., A. Kelbert, and G. D. Egbert (2015), Ionospheric current source modeling and global geomagnetic induction using ground geomagnetic observatory data, J. Geophys. Res. Solid Earth, 120, 6771–6796.

Telford, W., et al. (1990), Applied Geophysics Ed. 2, pp. 293–342.

Thiel, S., G. Heinson, A. Reid, and K. Robertson (2016), Insights into lithospheric architecture, fertilization and fluid pathways from AusLAMP MT, ASEG Ext. Abstr., 2016(1), 1–6, doi:10.1071/ASEG2016ab261.

Thomson, A. W. P., A. J. McKay, E. Clarke, and S. J. Reay (2005), Surface electric fields and geomagnetically induced currents in the Scottish Power grid during the 30 October 2003 geomagnetic storm, Space Weather, 3, S11002, doi:10.1029/2005SW000156.

Utada, H., and H. Munekane (2000), On galvanic distortion of regional three-dimensional magnetotelluric impedances, Geophys. J. Int., 140,385–398.

Van Rossum, G. (2011), The Python Language Reference Manual, edited by F. L. Drake Jr., published by Network Theory Ltd. ISBN 978-906966-14-0.

Vanhamaki, H., et al. (2013), Deriving the geomagnetically induced electric field at the Earth's surface from the time derivative of the vertical magnetic field, Earth Planets Space, 65, 997–1006.

Viljanen, A., et al. (1999), Modeling geomagnetically induced currents during different ionospheric situations, J. Geophys. Res., 104(28), 059–28,017.

Viljanen, A., et al. (2004), Fast computation of the geoelectric field using the method of elementary current systems and planar Earth models, Ann. Geophys., 22, 101–113.

Wait, J. (1962), Theory of magneto-telluric fields, J. Res. Natl. Bur. Stand., 66D, 509–541.

Wei, L., et al. (2013), Surface electric fields for North America during historical geomagnetic storms, Space Weather, 11, 451–462, doi:10.1002/swe.20073.

Weigel, R., D. Vassiliadis, and A. Klimas (2002), Coupling of the solar wind to temporal fluctuations in ground magnetic fields, Geophys. Res. Lett., 29, 1915, doi:10.1029/2002GL014740.

Yun, L., X. Xiaochun, L. Bin, and P. Jinfeng (2013), Time-frequency analysis based on the S-transform, Intl. J. of Signal Processing, Image Processing and Pattern Recognition, 6(5), doi:10.14257/ijsip.2013.6.5.22.

Zhang, T., and A. Schultz (1990), EXORCISE—An algorithm for detection of spurious values and prediction of missing data, Comput. Geosci., 16, 1027–1065.

Zhu, H. and T. Overbye (2015), Blocking Device Placement for Mitigating the Effects of Geomagnetically Induced Currents, IEEE Trans. Power Systems, 30(4), 2081 – 2089.